R. & M. No. 3600

MINISTRY OF TECHNOLOGY

AERONAUTICAL RESEARCH COUNCIL
REPORTS AND MEMORANDA

An Experimental and Theoretical Comparison at M = 4 of the Lift-to-Drag Ratio of some possible Aircraft Shapes

By C. S. BROWN and E. L. GOLDSMITH
Aerodynamics Dept., R.A.E., Bedford

LONDON: HER MAJESTY'S STATIONERY OFFICE
1969
PRICE 18*s.* 6*d.* NET

An Experimental and Theoretical Comparison at M = 4 of the Lift-to-Drag Ratio of some possible Aircraft Shapes

By C. S. BROWN and E. L. GOLDSMITH
Aerodynamics Dept., R.A.E., Bedford

Reports and Memoranda No. 3600*
March, 1967

Summary.

An experimental and theoretical comparison has been made between two different methods of combining excess cross-sectional area (due to the engine exhaust nozzle exit being larger than the intake entry) with the volume and lifting surface elements in an aircraft configuration.

Comparisons of measured and calculated values of $(L/D)_{max}$ have been made using linear theory and in general fair agreement is achieved. A systematic study of the effect of varying the proportions of the configurations studied leads to finding the optimum proportions for either approach.

LIST OF CONTENTS

*Replaces R.A.E. Technical Report 67 067—A.R.C. 29 415.

---

1. *Introduction.*

Design studies have shown that air-breathing engines are suitable for the propulsion of aircraft up to a Mach number of at least 7·0. It is possible therefore to consider aerodynamic vehicles at high supersonic speeds, in which the essential constituents are a volume for carrying the payload, a lifting surface having little or no stowage volume and nacelles which house the powerplant. In recent years a considerable amount of thought has been devoted to the problem of combining these elements into the most favourable combination, i.e. the one that gives the highest ratio of lift to drag in trimmed cruise flight.

One approach is to combine two or more of the elements into a single entity. For example thick slender wings can combine the lifting and stowage volume functions; or ducted wings may combine the functions of lifting surface and powerplant.

A second approach is to keep the elements identifiably separate, but to arrange them in positions relative to each other in such a way that they mutually interfere in a manner which enhances the lift to drag ratio.

Configurations that have half bodies underneath wings have been proposed for hypersonic boost glide vehicles[1], and these are good examples of a combination of the two approaches. The pressure drag associated with the stowage volume (the half body) is positioned so as to augment the undersurface lifting pressures on the wing; and the rocket nozzle (or equivalently the excess area of the exhaust over the inlet for an air-breathing engine) is integrated with the volume so that the body has no afterbody drag. Such configurations do not however have universal application owing to balance problems and a low ratio of stowage volume to wing area.

Using configurations that are more practical for aircraft which have to take off and land, and cruise at moderate or high supersonic speeds, Goldsmith and Cook[2] have tried to establish the order of gain in lift to drag ratio obtainable from the use of interference principles. In the present Report one of the configurations studied in Ref. 2 is made the basis of a specific comparison of the two approaches. The basic wing-body combination is shown in Fig. 1a. Figs. 1b, 1c and 1d show propulsion units of different form added to this arrangement. Integration of the powerplant with the payload-carrying volume as shown in Fig. 1b should lead to a reduction in the overall pressure drag. This principle has been discussed by Squire[3].

The favourable interference approach is shown in Figs. 1c and 1d, where the afterbody associated with the payload-carrying volume is placed wholly on top of the wing, while the duct for the propulsion unit grows from its inlet area to the larger exhaust area wholly under the wing. This produces a configuration

with a higher drag than the basic wing and body, but with favourable lifting pressures induced on both top and bottom surfaces of the wing.

Because conditions inside the duct were not relevant to this experiment, and to simplify manufacture, the engine inlet area is not reproduced on the models. Only the excess of nozzle exit area over engine inlet area is represented, and this has been assumed in all cases equal to the maximum cross-sectional area of the basic body. The models are therefore as shown in Figs. 1e to 1h, although they are representative of the configurations illustrated in Figs. 1b to 1d.

Measurements have been made of lift, drag and pitching moment on comparable models designed in the manner outlined above. Calculations have been made to indicate under what geometric conditions the two approaches show advantage relative to each other. A comparison has been drawn between the various methods of integrating the propulsion unit and also with the configuration represented in Fig. 1j, in which the engines are attached to the wings without any consideration of integration or favourable interference.

2. *Experimental Details.*

2.1. *Details of Models Tested.*

Details of the bodies used in these tests are given in Fig. 2a. All have been derived from the basic shape (Fig. 1a) by the addition of excess engine exit area equal to the maximum cross-sectional area of the body, as explained in the introduction and shown in Fig. 1. Thus B_1 is the idealised integrated version with parallel afterbody resulting from the symmetrical disposition of the excess exit area. B_2 is an alternative version, which is more realistic, where the base area is all placed above the lifting surface. Thus although the afterbody remains of constant cross-sectional area there is a change in cross-sectional shape from circular to semi-circular. Bodies B_3, B_4 and B_5 are representative of the interference approach. The after-body is above the lifting surface and produces both lift and drag. The engine is placed under the wing so that the pressures associated with the nacelle drag also produce an additional lift force on the wing. The difference between the three bodies, B_3, B_4 and B_5 is in the shape of the underbody, which would be dictated by the shape of the intake. Bodies B_3 and B_4, in which the front of the underbody is respectively a horizontal wedge and a vertical wedge, are consistent with the equivalent versions of a rectangular intake (*see* Fig. 1). The underbody B_5 represents a semicircular intake.

In every case the combined cross-sectional area of afterbody and underbody remains constant and equal to the maximum cross-sectional area of the basic body. Details of the afterbodies and underbodies are given in Figs. 2b, 2c and 2d.

Each body can be fitted with any of three different wings, details of which are shown in Fig. 3. Apart from the chamfered leading edges the wings are of constant thickness with blunt trailing edges.

2.2. *Test Facility.*

The tests were carried out in the 3 feet × 4 feet, high supersonic speed tunnel at the R.A.E., Bedford during 1964. This is a variable density, continuous flow tunnel, which at the time of these experiments was fitted with a fixed wooden nozzle providing a Mach number of 4. The tunnel has been described in Ref. 4.

2.3. *Measurements.*

Strain-gauge balance measurements of lift, drag, and pitching moment were made on all configurations over an incidence range of $-4°$ to $10°$.

Stagnation pressure was 110 pounds per square inch absolute and stagnation temperature 40°C, giving a Reynolds number based on total model length of $2{\cdot}8 \times 10^7$. The humidity of the air in the tunnel was kept at 100 to 150 parts per million by weight.

Base pressures were measured on all bodies. The base of each body was recessed in accordance with the recommendation of Ref. 5 and pressures were measured using pitot tubes arranged as in Fig. 4. The body base drag was computed using the average base pressure and has been subtracted from the total axial force.

In general no corresponding adjustment has been made for wing base pressure. Base pressures were measured on wings W_1 and W_2 by means of tubes let into, and flush with, the bluff base. The pressures have been used to facilitate comparison between calculated and measured values of drag (*see* Section 4.2).

In order to check the condition of the boundary layer, the sublimation technique[6] was used to give a visual indication of boundary-layer transition. The models were sprayed with a solution of acenaphthene in acetone. The tunnel running time required for transition indication was about ten to fifteen minutes. Configurations $B_1\ W_1$ and $B_1\ W_3$ were tested at zero incidence over a range of Reynolds number, and a series of typical patterns is given in Fig. 5. The results of measurements made from these photographs are plotted in Fig. 6, where transition Reynolds number is based on the chordwise distance from the leading edge of the wing to the mean transition line as indicated on the photographs. Some results from Ref. 7 are also shown for comparison. As a result of these measurements the force tests were carried out with a band of No. 60 carborundum particles 0·1 inch wide and 0·03 inch high, placed around the body 1·5 inches from the nose. No roughness was put on the wings.

2.4. *Accuracy.*

Balance and pressure measurement accuracies lead to uncertainties in the various components as follows:

C_L	C_D	C_M	L/D	X_p/l
$\pm 0{\cdot}004$	$\pm 0{\cdot}0001$	$\pm 0{\cdot}0002$	$\pm 0{\cdot}04$	$\pm 0{\cdot}003$

All force and moment coefficients are based on gross wing area, i.e. the area of the planform shown in Fig. 3.

Angles of incidence are estimated to be accurate to $\pm 0{\cdot}05$ deg.

3. *Experimental Results.*

The results of base pressure measurements on bodies B_1, B_2 and B_5, in combination with wings W_1 and W_3 are shown in Fig. 7.

Lift, drag and pitching-moment coefficients, together with centre of pressure location, are presented as a function of angle of incidence in Figs. 8 to 16. Lift to drag ratios have been derived and are plotted in Fig. 17. The maximum values of lift to drag ratio for all configurations are summarised in Table 1.

The experimental lift to drag ratios for all wings in combination with body B_1 are shown plotted against aspect ratio and $\tau\left(=\dfrac{\text{volume}}{(\text{plan area})^{3/2}}\right)$ in Fig. 18. Results from Ref. 8 are shown for comparison. These results were obtained at $M = 2{\cdot}94$ on a series of wing-body combinations similar to configurations using B_1. It will be noted that whereas in Ref. 8 $(L/D)_{\max}$ decreased with increase in aspect ratio as the wing leading edge changed from sonic to supersonic, this feature is not repeated in the present tests. Apart from this, the descrepancy between the two sets of results can be ascribed largely to difference in Mach number.

4. *Theoretical Maximum Lift-Drag Ratio.*

4.1. *General.*

In Ref. 9, Migotsky and Adams propose a simple theory for estimating the maximum lift-drag ratio of a body mounted under a triangular wing. This gives

$$\left(\frac{L}{D}\right)_{\max} = \pm \frac{\dfrac{dC_L}{d\alpha}}{2\sqrt{C_{D_0}\dfrac{dC_L}{d\alpha} - C_{L_0}\,G \mp C_{L_0} \pm G}} \tag{1}$$

in which the upper signs correspond to the body under the wing and the lower signs refer to the inverted configuration.

In the same reference it is also shown that for a full cone mounted symmetrically on a triangular wing the optimum lift-drag ratio reduces to:

$$\left(\frac{L}{D}\right)_{\max} = \frac{1}{2}\sqrt{\frac{dC_L/d\alpha}{C_{D_0}}} \tag{2}$$

Goldsmith and Cook[2] have extended this work slightly and applied it to several types of interference configuration to predict values of maximum lift-drag ratio in reasonable agreement with measured values for slender half bodies beneath sonic leading edge delta wings. Using similar methods it is possible to estimate the values of the various components of equation (1) for the present configurations. These can then be compared with the experimental values derived from Figs. 8 to 13.

4.2. *Estimation of Components in Equation* (1).

C_{D_0}

In order to obtain a value of the drag at zero incidence which can be compared directly with the experimental values, it is necessary to include the effect of wing leading-edge bluntness and wing base pressure, as well as the wing-body skin friction and pressure drags.

The effect of leading-edge bluntness has been taken simply as the pressure behind a normal shock acting on the leading-edge area; while the wing base pressures were obtained from Fig. 7. Skin-friction drag has been calculated by the method of Ref. 10.

Except for the underbodies representing the propulsion units on B_3, B_4 and B_5, estimates of the pressure drag of the wings and bodies are based on charts given in Refs. 11 and 12 respectively. For the quasi-wedge shaped underbodies on B_3 and B_4 surface pressures have been estimated assuming oblique shock wave relations; corrections were made for changes in the local pressure behind the Mach lines emanating from the leading-edge tips. The underbody on B_5 has been assumed to be a half cone and the pressure drag was again obtained from Ref. 12.

In Table 3 the calculated and experimental values of C_{D_0} are shown for all configurations. A detailed breakdown of the components of C_{D_0} for configurations $B_1\,W_1$ and $B_5\,W_1$ is given in Table 4.

C_{L_0}

Values of C_{L_0} due to fuselage afterbody and propulsion unit underbody have been estimated for B_3, B_4 and B_5 by using the expression given in Ref. 2, i.e.

$$C_{L_0} = \frac{2}{\beta}\cdot\frac{S_b}{S_W}. \tag{3}$$

These estimates are given in Table 3, together with the experimental results obtained from Figs. 8, 9 and 10.

In the case of body B_5 the underbody is very nearly conical and the lift induced on the wing can be obtained by integrating the pressure field about a cone over the area of the wing which it affects. Results obtained in this way are about six per cent lower than those given by equation (3), which is in general agreement with the trends shown in Fig. 4 of Ref. 2.

Some indication of the relative extent of the interference effect on the three different wings W_1, W_2 and W_3, due to the conical underbody, can be obtained from Fig. 19a.

G

The quantity G is the rate of change of axial force with incidence and is due mainly to the effect of the pressure field of the wing at incidence, acting on the surface of the body. The assumption has been

made that the pressure acting on the body is constant over the body and equal to the pressure along the centre line of the wing as obtained from linear theory for the wing alone.

Thus for a supersonic leading edge wing (e.g. wings W_1 and W_2)

$$G = \frac{\tan \lambda}{\sqrt{\beta^2 \tan^2 \lambda - 1}} \cdot \cos^{-1}\left[\frac{1}{\beta \tan \lambda}\right] \cdot \frac{4}{\pi} \cdot \frac{S_b}{S_W} \tag{4}$$

and for a wing with subsonic leading edge (e.g. wing W_3)

$$G = \frac{2 \tan \lambda}{E(K')} \cdot \frac{S_b}{S_W}. \tag{5}$$

In equation (5), E is a complete elliptical integral of the second kind in which $K' = \sqrt{1-K^2}$; $K = \beta \tan \lambda$.

These results for G are tabulated, together with the experimental values, in Table 3.

Lift-curve slope

The values of lift-curve slope for the wing-body combinations, which are given in Table 3, were obtained by using the method of Ref. 13. Lift-curve slope is shown plotted against tangent ratio ($\tan \lambda / \tan \mu$) in Fig. 20a, together with the linear theory values of $dC_L/d\alpha$ for a delta wing alone at $M = 4{\cdot}0$. The increment due to the body alone based on Ref. 14 is also shown.

4.3. *Evaluation of Maximum Lift to Drag Ratio.*

The values of C_{D_0}, C_{L_0}, G and $dC_L/d\alpha$, obtained by the methods of Section 4.2, have been inserted in equation (1) in the case of asymmetric configurations and in equation (2) for symmetric configurations, in order to obtain theoretical values of the maximum lift-drag ratios. These results have been summarised in Table 2 for all configurations.

5. *Discussion.*

5.1. *Comparison of Experimental and Established Results.*

Table 3 shows that, by using the simple methods of Section 4, very fair agreement can be obtained between estimates and experimental results for the drag and lift at zero incidence.

Unfortunately, good agreement does not extend to the lift-curve slope, for which the simple method overestimates and as Fig. 20a shows, this is particularly so in the cases of wings W_1 and W_2. This result, however, is consistent with previous experience on delta wings alone[15, 16] where it has been found that at values of the tangent ratio close to those for shock detachment, the experimental values of lift-curve slope fall below linear theory predictions. In Fig. 20b the parameter $\left(\frac{dC_L}{d\alpha} \cdot \frac{\beta}{4}\right)$, obtained in the present tests with wings in combination with body B_1, is seen to be in very good agreement with the experimental results of Ref. 8.

With the exception of those configurations involving wings W_3 and body B_2, the agreement between calculated and experimental values of the maximum lift-drag ratio is quite good. The disagreement in the case of wing W_3 is largely due to the overestimation in lift-curve slope value. In the case of body B_2 the discrepancy can be accounted for by the fact that experiment shows a non-zero value for the term G. From the simple concept of G, with constant afterbody cross-sectional area and therefore no net forward facing area, this term should be zero. However, although the afterbody has a constant cross-sectional area, it changes shape from circular at its upstream junction with the parallel centre body to semicircular at the base. Therefore between successive cross sections there is a forward facing area adjacent to the wing and a rearward area at the top of the body remote from the wing, as shown in Fig. 19b. Pressure differences in the wing flow field over these areas could cause a noticeable change of axial force with incidence. How-

ever, as can be seen from Table 3, numerical integration of these pressures yields a value of G which is only about ten per cent of that found by experiment.

5.2. *Comparison of the Two Methods of Utilising the Excess Cross-Sectional Area.*

Bodies B_1 and B_5 provide a direct comparison between the two methods of using the excess nozzle area which were outlined in the introduction. In the former the excess area is integrated with the payload carrying volume as in Fig. 1e, and in the latter it is added in an interference manner corresponding to Fig. 1f.

It can be seen from Tables 1 and 2 that the maximum lift to drag ratios found from experiment confirm the simple estimates in that, for the particular bodies used in these tests, the method of Fig. 1e (integration) is better, although the advantage, as was to be expected, is not great, being only about three to six per cent. Indeed if one considers that B_2 may be a more realistic alternative to B_1, then the experimental results suggest that there is no real advantage in integration.

By applying the estimation methods of Section 4 to the types of configuration shown in Figs. 1e and 1f the comparison can be extended to configurations whose proportions are different from those tested. In this way the effect of changing forebody and afterbody fineness ratios, and of varying the proportion of the base area above and below the wing have been investigated and the results are given in Fig. 21.

In the Appendix, equations (1) and (2) of Section 4.1 have been used to show that the maximum lift to drag ratio of the two configurations, Figs. 1e and 1f, will be approximately equal when:

$$\frac{\Delta}{\sqrt{C_{D_0}}} = a \tag{6}$$

where C_{D_0} is the zero incidence drag of the integrated configuration, Δ is the difference in zero-incidence drag between the two configurations and $a = C_{L_0} - G$, i.e. a measure of the interference effect.

Now reference to equations (3) and (4) of Section 4.2 shows that this interference effect is independent of the length of the afterbody. Therefore, for a given base area, equation (6) indicates that improvement in an interference configuration over the corresponding integrated configuration will be obtained only by reducing Δ. All other drag components being equal, a reduction in Δ implies a reduction in afterbody drag, which can only be brought about by increasing the afterbody fineness ratio. The question at issue therefore is whether the afterbody fineness ratio can be increased to the point at which the difference in zero-incidence drag between the corresponding configurations becomes less than the interference effect as defined by a. In Fig. 21a, maximum lift-drag ratio based on equation (1) is plotted against afterbody fineness ratio for various values of forebody fineness ratio. These calculations assume in all cases a sonic leading edge wing with a centreline chord equal to the afterbody length. This means that none of the model configurations is, in fact, exactly represented. This assumption, however, enables the maximum interference effect to be obtained for each value of afterbody length. As can be seen, the afterbody fineness ratio can be increased to the point where the interference version is better than the integrated version; the advantage however is only about two per cent.

The effect of increasing forebody fineness ratio is to reduce C_{D_0} without change in Δ or in the interference effect a. It follows therefore from equation (6) that advantage of the integrated configuration is enhanced. Fig. 21b confirms this trend in the case of $B_1\ W_1$ and $B_5\ W_1$. In this figure values of $(L/D)_{max}$ based on equation (1) are plotted against forebody fineness ratio; the fineness ratios of the afterbody and the parallel centre body being kept constant and equal to the values used on the models (*see* Fig. 2). The points on the curves corresponding to configurations $B_1\ W_1$ and $B_5\ W_1$ are clearly marked. Values of $(L/D)_{max}$ for the basic wing-body combination (Fig. 1a) and for the configuration shown in Fig. 1j (where no attempt is made to utilise excess exit area) have also been calculated and are shown.

It can be seen that for the particular configurations investigated, adding the powerplant in an integration fashion actually gives a slight improvement on the $(L/D)_{max}$ of the basic wing and body.

Compared with the basic wing and body with powerplant added as wing mounted nacelles (Fig. 1j) the benefit of integration is about nine per cent and the benefit due to a favourable interference layout is about four per cent.

It should be noted that the difference between the $(L/D)_{max}$ values given in Figs. 21a and 21b for any particular body is due to the fact that in the two cases different wings are associated with the body resulting in different values of the volume parameter τ.

In Fig. 21c, $(L/D)_{max}$ is plotted against the proportion of base area below the wing for various body configurations in combination with wing W_1. Here the fineness ratio of the parallel centre body has again been kept constant at the model value of 3·62. The calculations have been carried out using two different values of the afterbody fineness ratio; 5·76, (the model ratio) and 7·43. Forebody fineness ratio has also been varied from the model value of 3, to 9. The curve for forebody fineness ratio equal to 3 therefore shows the effect of the transition from configuration $B_2\ W_1$ which has all the base area above the wing, to configuration $B_5\ W_1$, which is the corresponding interference version and in which the base area is all below the wing.

Clearly in all these curves there is no optimum base area distribution between the two end points and the relation between the two end points depends only on the particular afterbody fineness ratio chosen as was seen in Fig. 21a.

6. *Conclusions.*

An experimental and theoretical comparison has been made between the integration and interference methods of combining the propulsion unit with the volume and lifting elements in an aircraft configuration. The main conclusions are as follows:

1. The idealised integrated version is shown to have the highest $(L/D)_{max}$ both theoretically and experimentally and this $(L/D)_{max}$ is in excess of that for the basic combination of wing and body only.
2. The difference between a practical integrated version and an interference version is very small.
3. It has been shown by calculation that, by increasing the fineness ratio of the afterbody and tailoring the wing shape to the afterbody and propulsion unit pressure fields, it should be possible to design the interference version to give a slightly higher $(L/D)_{max}$ than the idealised integrated version.
4. Estimation of C_{L_0}, C_{D_0} and $dC_L/d\alpha$ by linear theory methods gives fair agreement with measurements for most configurations. Increasing errors in lift-curve slope, as aspect ratio decreases, lead directly to similar errors in estimating $(L/D)_{max}$.

Acknowledgement.

The authors gratefully acknowledge the help given by Mr. J. G. Jones who conceived this series of tests and designed the models.

LIST OF SYMBOLS

a	$(C_{L_0} - G)$
A	Aspect ratio
b	Wing span
C	Centreline chord of wing
C_D	Drag coefficient $\frac{D}{q_\infty S_W}$
C_{D_0}	Drag coefficient at zero incidence
C_L	Lift coefficient $\frac{L}{q_\infty S_W}$
C_{L_0}	Lift coefficient at zero incidence
C_M	Pitching-moment coefficient about body base $\frac{\text{pitching moment}}{q_\infty . S_W . l}$
C_X	Axial-force coefficient $\frac{X}{q_\infty S_W}$
d	Maximum diameter of body
G	Rate of change of axial force with incidence $\frac{dC_X}{d\alpha}$
L	Lift
l	Body length
l_A	Length of afterbody
l_P	Length of parallel portion of body
l_F	Length of forebody
M	Mach number
p_∞	Free-stream static pressure
p_b	Base pressure
q_∞	Free-stream dynamic pressure
R	Reynolds number based on model length

LIST OF SYMBOLS—*continued*

S_b	Cross-sectional area of base of body
S_W	Gross wing area
t	Wing thickness
X	Axial force
X_p	Centre of pressure measured from vortex of body nose
y	Spanwise distance from wing centreline
α	Angle of incidence
β	$\sqrt{M^2-1}$
Δ	Difference between zero incidence drag of corresponding integrated and interference configurations based on Figs. 1e and 1f
λ	Semi apex angle of wing $= 90° - \Lambda$
μ	Mach angle
Λ	Sweepback angle of wing
ψ	Angle of wing leading edge, normal to leading edge
τ	$\frac{\text{Volume}}{(\text{planform area})^{3/2}}$: a volume parameter

REFERENCES

No.	*Author(s)*	*Title, etc.*
1	A. J. Eggers and C. A. Syvertson	Aircraft configurations developing high lift-drag ratios at high supersonic speeds. NACA/TIL/5007. A.R.C. 18632 (1956).
2	E. L. Goldsmith and P. H. Cook . .	Half-body and wing combinations in supersonic flow. A review of some principles and possibilities. A.R.C., R. & M. 3528.
3	L. C. Squire	The use of excess engine exit area over intake area to reduce zero-lift drag at high supersonic speeds. R.A.E. Technical Note Aero 2940, (A.R.C. 25838) (1963).
4	J. Poole	A description of the R.A.E. high supersonic speed tunnel. R.A.E. Technical Note Aero 2678 (1960).
5	D. F. Hasson and J. G. Presnell	Static lift, drag and pitching-moment characteristics of wings with arrow and modified-diamond planforms combined with several different bodies at Mach numbers of 2·97, 3·35 and 3·71. NASA/TIL/6372 (1959).
6.	J. D. Main-Smith	Chemical solids as diffusable coating films for visual indication of boundary layer transition in air and water. A.R.C., R. & M. 2755 (1950).
7	S. R. Pate and R. E. Brillhart	Investigation of boundary layer transition on swept wings at Mach numbers of 2·5 to 5. AEDC-TDR-63-109 (1963).
8	L. H. Jorgensen	Experimental lift-drag ratios for two families of wing-body combinations at supersonic speeds. NACA RM A58A08 (1958).
9	E. Migotsky and G. J. Adams	Some properties of wing and half-body arrangements at supersonic speeds. NACA RM A57E15 (1957).
10	K. G. Smith	Methods and charts for estimating skin-friction drag in wind tunnel tests with zero heat transfer. A.R.C., C.P. 824 (1964).
11	R. A. Bishop and E. G. Cane	Charts of the theoretical wave drag of wings at zero-lift. A.R.C., C.P. 313 (1956).
12	L. E. Fraenkel	The theoretical wave drag of some bodies of revolution. A.R.C., R. & M. 2842 (1951)
13	—	Royal Aeronautical Society. Data Sheets. Aerodynamics Vol. 3.

REFERENCES—*continued*

No.	*Author(s)*	*Title, etc.*
14	—	Royal Aeronautical Society. Data Sheets. Aerodynamics Vol. 4.
15	E. F. Ulmann and M. H. Bertram	Aerodynamic characteristics of low aspect ratio wings at high supersonic Mach numbers. NACA RM L53I23 (1953).
16	E. S. Love	Investigations at supersonic speeds of 22 triangular wings representing two airfoil sections for each of 11 apex angles. NACA Report 1238 (1955).

APPENDIX

Comparison of the Maximum Lift-Drag Ratios of Corresponding Integrated and Interference Configurations Based on the Equations of Section 4.1

For the integrated configuration (Fig. 1e):

$$\left(\frac{L}{D}\right)_{\max} = \frac{1}{2}\sqrt{\frac{\frac{dC_L}{d\alpha}}{C_{D_0}}} = \frac{\frac{dC_L}{d\alpha}}{2\sqrt{C_{D_0}\cdot\frac{dC_L}{d\alpha}}} \tag{A.1}$$

and for the corresponding integrated configuration (Fig. 1f):

$$\left(\frac{L}{D}\right)_{\max} = \frac{\frac{dC_L}{d\alpha}}{2\sqrt{C'_{D_0}\frac{dC_L}{d\alpha} - C_{L_0}\cdot G - C_{L_0} + G}} \tag{A.2}$$

where C'_{D_0} is the zero-incidence drag of the interference configuration and will be greater than C_{D_0} which is the zero-incidence drag of the integrated version. The maximum lift-drag ratio is therefore the same for each configuration when

$$\frac{\frac{dC_L}{d\alpha}}{2\sqrt{C_{D_0}\cdot\frac{dC_L}{d\alpha}}} = \frac{\frac{dC_L}{d\alpha}}{2\sqrt{C'_{D_0}\frac{dC_L}{d\alpha} - C_{L_0}\cdot G - C_{L_0} + G}}. \tag{A.3}$$

In most of the calculations carried out on the configurations referred to in the text it has been found that $(C_{L_0}\cdot G)$ is small enough to be neglected in comparison with $\left(C_{D_0}\cdot\frac{dC_L}{d\alpha}\right)$; and that $\frac{dC_L}{d\alpha}$ is very nearly unity. With these assumptions equations (A.3) reduces to

$$\frac{1}{2\sqrt{C_{D_0}}} = \frac{1}{2\sqrt{C'_{D_0} - C_{L_0} + G}}. \tag{A.4}$$

Let

$$\Delta = C'_{D_0} - C_{D_0}$$

the difference in zero-incidence drag between corresponding integrated and interference configurations.

And let

$$a = C_{L_0} - G$$

which is the important interference effect parameter.

Equation (A.4) can now be rewritten,

$$\frac{1}{2\sqrt{C_{D_0}}} = \frac{1}{2\sqrt{C_{D_0} + \Delta - a}} \tag{A.5}$$

from which

$$\left(1+\frac{\Delta}{C_{D_0}}\right)^{\frac{1}{2}}-1=\frac{a}{2\sqrt{C_{D_0}}}. \tag{A.6}$$

Now

$$\left(1+\frac{\Delta}{C_{D_0}}\right)^{\frac{1}{2}}=1+\frac{\Delta}{2C_{D_0}}$$

ignoring higher powers of $\frac{\Delta}{C_{D_0}}$ and substitution in equation (A.6) gives

$$\frac{\Delta}{\sqrt{C_{D_0}}}=a\,. \tag{A.7}$$

Summary of $(L/D)_{max}$ for all Configurations

TABLE 1

Experimental Values

Body \ Wing	W_1	W_2	W_3
B_1	5·49	5·24	4·90
B_2	5·27	4·95	4·80
B_3	5·16	4·90	4·68
B_4	4·99	4·79	4·76
B_5	5·18	5·10	4·76

TABLE 2

Estimated Values

Body \ Wing	W_1	W_2	W_3
B_1	5·68	5·44	5·35
B_2	5·67	5·43	5·32
B_3	5·19	5·04	5·02
B_4	5·00	4·83	4·75
B_5	5·40	5·29	5·26

TABLE 3

Comparison of Estimated and Experimental Values of C_{D_0}, C_{L_0}, G and $dC_L/d\alpha$

	C_{D_0}		C_{L_0}		G		$dC_L/d\alpha$	
	Estimated	Experimental	Estimated	Experimental	Estimated	Experimental	Estimated	Experimental
$B_1 W_1$	0·0085	0·0094	0	0	0	0	1·10	1·15
$B_1 W_2$	0·0093	0·0099	0	0	0	0	1·10	1·01
$B_1 W_3$	0·0093	0·0098	0	0	0	0	1·06	0·92
$B_2 W_1$	0·0085	0·0095	0	0	0·00032	0·0119	1·10	1·22
$B_2 W_2$	0·0093	0·0104	0	0	0·00063	0·0075	1·10	1·11
$B_2 W_3$	0·0093	0·0104	0	0	0·00094	0·0119	1·06	1·02
$B_3 W_1$	0·0114	0·0112	0·0288	0·0232	0·0225	0·0306	1·10	1·13
$B_3 W_2$	0·0129	0·0119	0·0382	0·0310	0·0263	0·0306	1·10	1·00
$B_3 W_3$	0·0134	0·0121	0·0444	0·0331	0·0284	0·0306	1·06	0·93
$B_4 W_1$	0·0122	0·0113	0·0288	0·0211	0·0225	0·0279	1·10	1·17
$B_4 W_2$	0·0140	0·0126	0·0382	0·0286	0·0263	0·0279	1·10	1·00
$B_4 W_3$	0·0147	0·0122	0·0444	0·0371	0·0284	0·0279	1·06	0·92
$B_5 W_1$	0·0106	0·0112	0·0288	0·0244	0·0225	0·0252	1·10	1·12
$B_5 W_2$	0·0119	0·0114	0·0382	0·0304	0·0263	0·0252	1·10	1·00
$B_5 W_3$	0·0124	0·0119	0·0444	0·0351	0·0284	0·0252	1·06	0·95

TABLE 4

Estimated Components of C_{D_0} for Configurations $B_1\ W_1$ and $B_5\ W_1$

			$B_1\ W_1$	$B_5\ W_1$
Pressure drag	Wing		0·00016	0·00016
	Wing base pressure		0·00136*	0·00136*
	Wing leading edge bluntness		0·00088	0·00088
	Forebody		0·00236	0·00236
	Afterbody		—	0·00056
	Interference Effect of forebody on afterbody		—	0·00032
	Nacelle		—	0·00081
Skin friction		Body	0·00152	0·00185
		Wing	0·00226	0·00226
		$C^D{}_0$	0·00854	0·01056

*Measured values

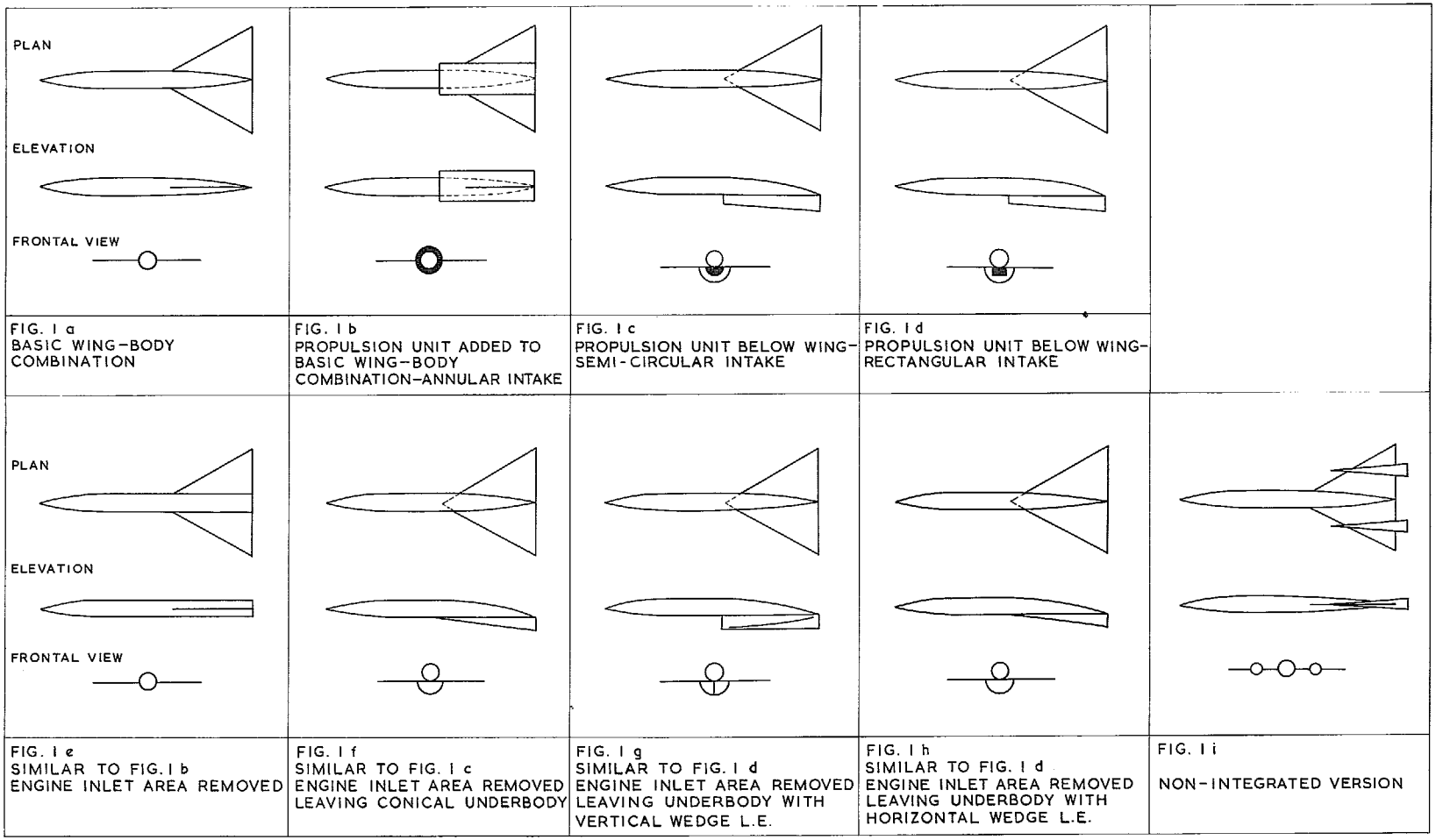

FIGS. 1a to j.

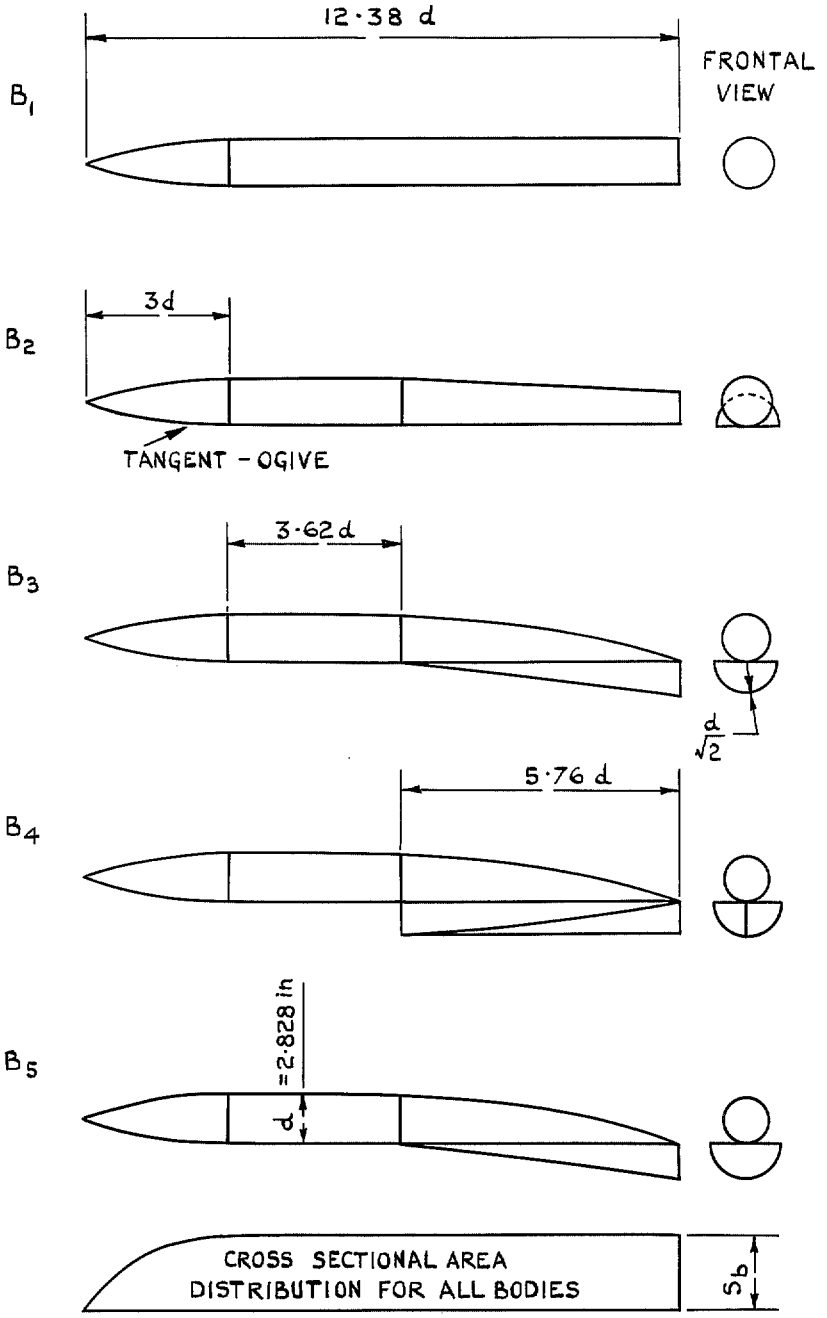

FIG. 2a. Body Details.

B_2 AFTERBODY

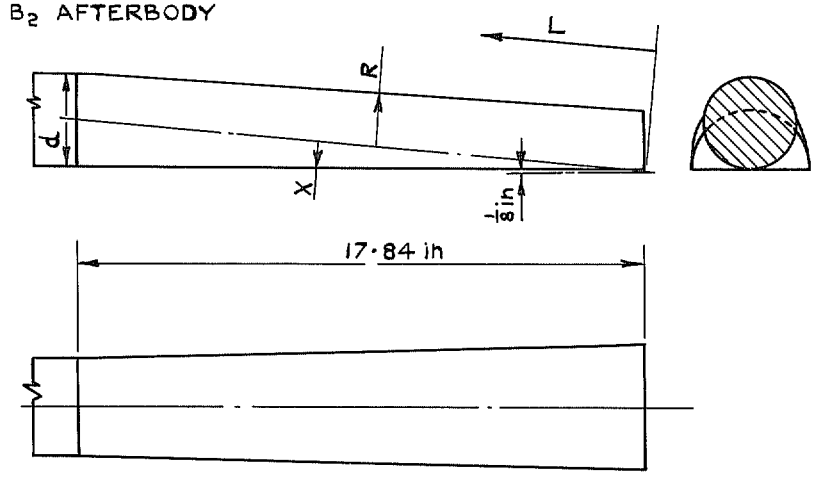

L	0	2·079	3·954	5·653	7·201	8·617	9·914	11·10	12·19	13·19	14·09	14·91	15·63	16·26	16·79	17·21	17·46	17·72	
X	0	0·165	0·314	0·449	0·573	0·685	0·788	0·883	0·970	1·049	1·121	1·185	1·243	1·293	1·335	1·369	1·393	1·409	
R	2	1·898	1·811	1·737	1·674	1·621	1·577	1·539	1·508	1·483	1·463	1·447	1·435	1·426	1·420	1·417	1·415	1·414	

B_3 B_4 B_5 AFTERBODY (UPPER)

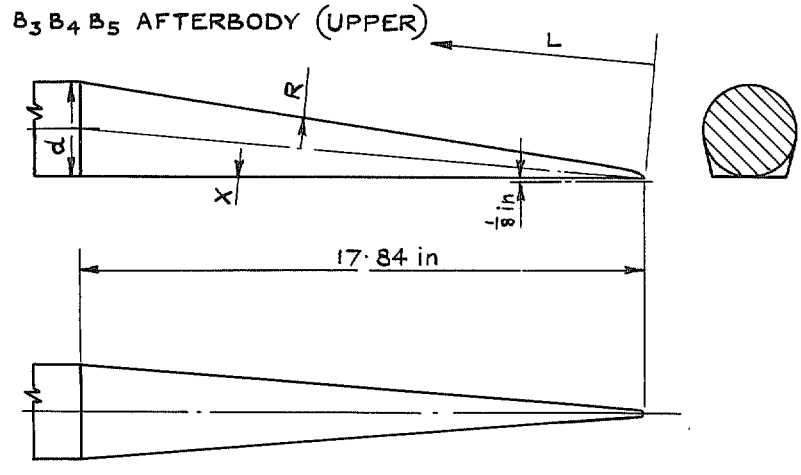

L	0·243	0·879	1·797	2·916	4·175	5·527	6·932	8·360	9·780	11·17	12·49	13·73	14·86	15·84	16·66	17·27	17·65		
X	0·019	0·070	0·143	0·232	0·332	0·439	0·551	0·665	0·778	0·888	0·994	1·092	1·182	1·260	1·324	1·373	1·404		
R	0·222	0·403	0·552	0·678	0·786	0·879	0·961	1·034	1·100	1·159	1·213	1·261	1·304	1·341	1·371	1·394	1·409		

FIG. 2b. Afterbody ordinates.

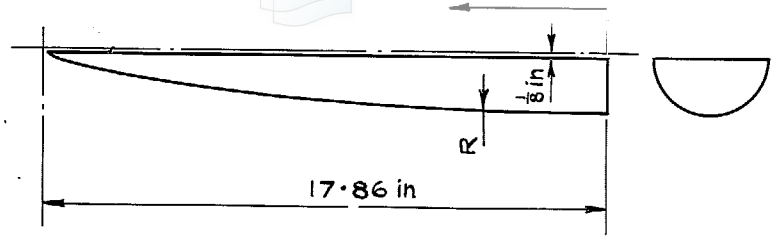

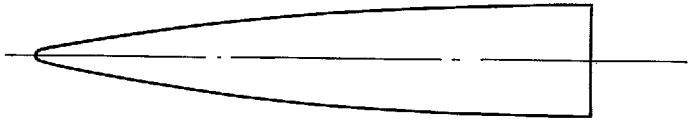

L	0	1	2	3	4	5	6	7	8	9	10	11	12
R	2·0	1·943	1·884	1·824	1·762	1·697	1·630	1·560	1·486	1·409	1·327	1·240	1·146

L	13	14	15	16	17	17·2	17·4	17·6	17·7	17·75	17·8	17·86	
R	1·043	0·930	0·800	0·645	0·439	0·385	0·321	0·241	0·189	0·157	0·116	0	

B_4 UNDERBODY

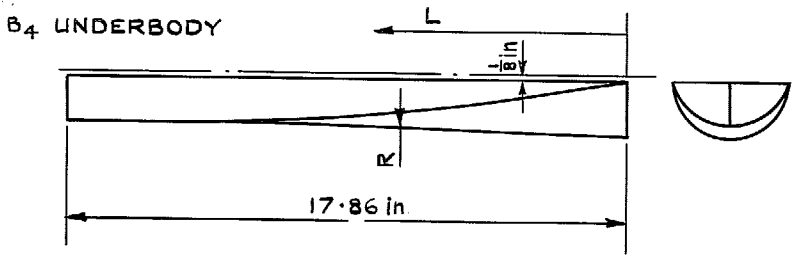

L	0	1	2	3	4	5	6	7	8	9	10	11	12	13	14	15	16	17	17·86
R	2·0	1·944	1·895	1·852	1·814	1·780	1·750	1·723	1·699	1·677	1·657	1·638	1·622	1·608	1·595	1·585	1·577	1·572	1·571

FIG. 2c. Afterbody Ordinates.

B_3 UNDERBODY

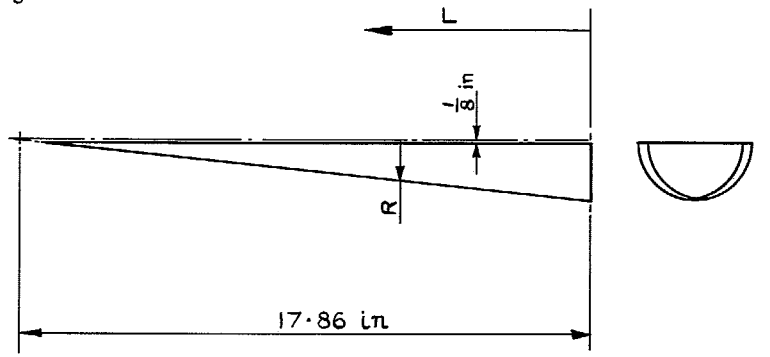

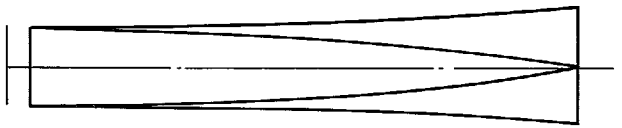

L	0	1	2	3	4	5	6	7	8	9	10	11	12	13	14	15	16	17	17·86
R	2·0	1·944	1·895	1·852	1·814	1·780	1·750	1·723	1·699	1·677	1·657	1·638	1·622	1·608	1·595	1·585	1·577	1·572	1·571

FIG. 2d. Afterbody ordinates.

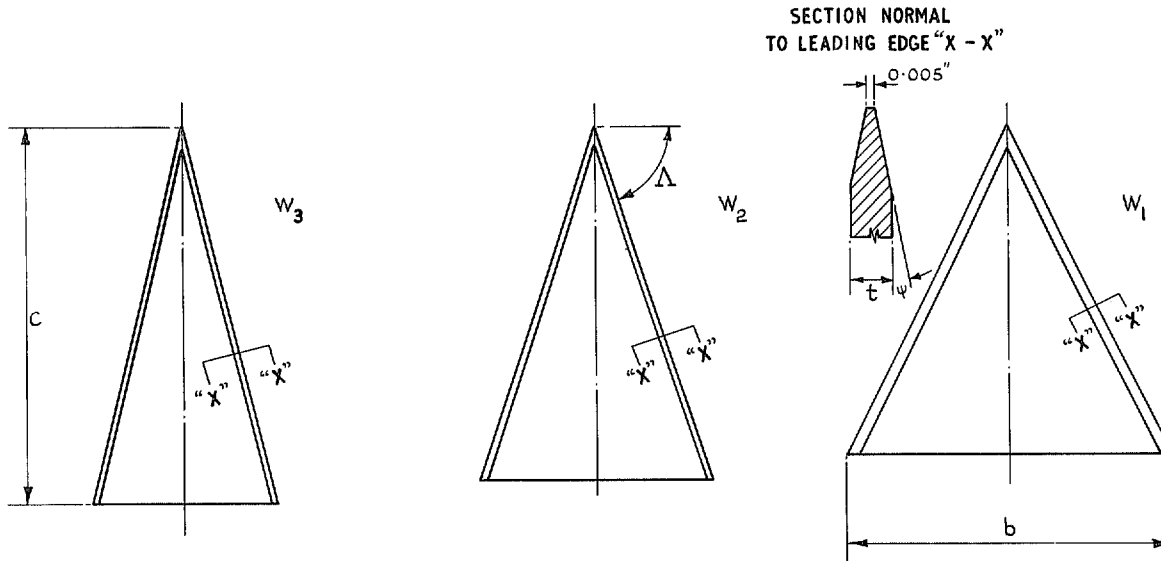

WING	c	b	Λ	t	ψ	S_w	A
W_1	21"	21"	63·4°	0·25"	11°	220·5	2
W_2	22·57"	15·05"	71·6°	0·25"	15·5°	169·8	$\frac{4}{3}$
W_3	24·14"	12·07"	76·0°	0·25"	20°	145·7	1

FIG. 3. Wing details.

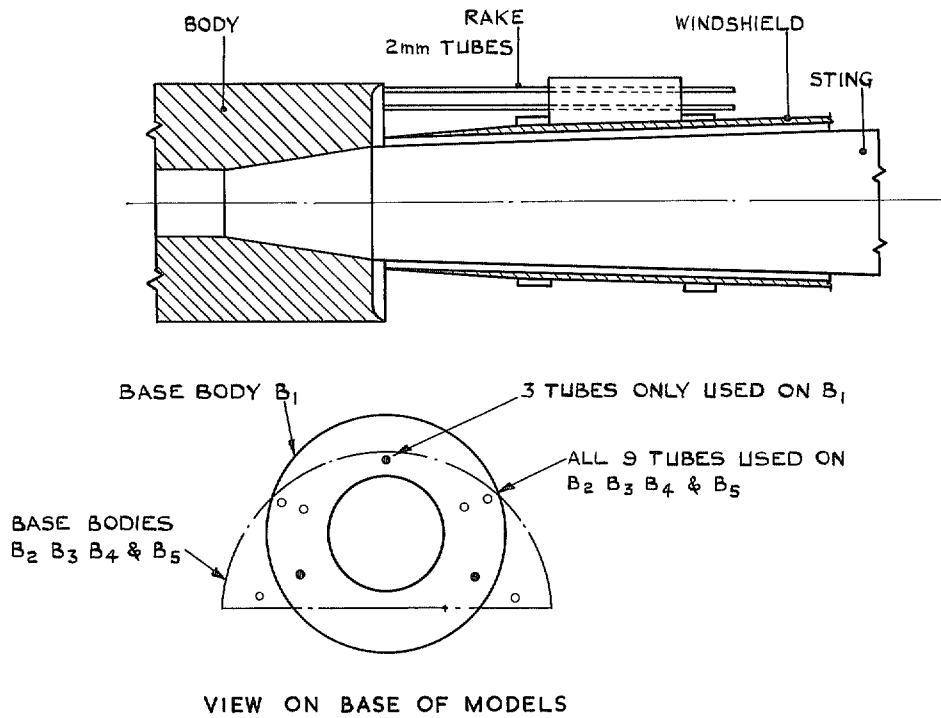

FIG. 4. Location of pitots for measuring body base pressures.

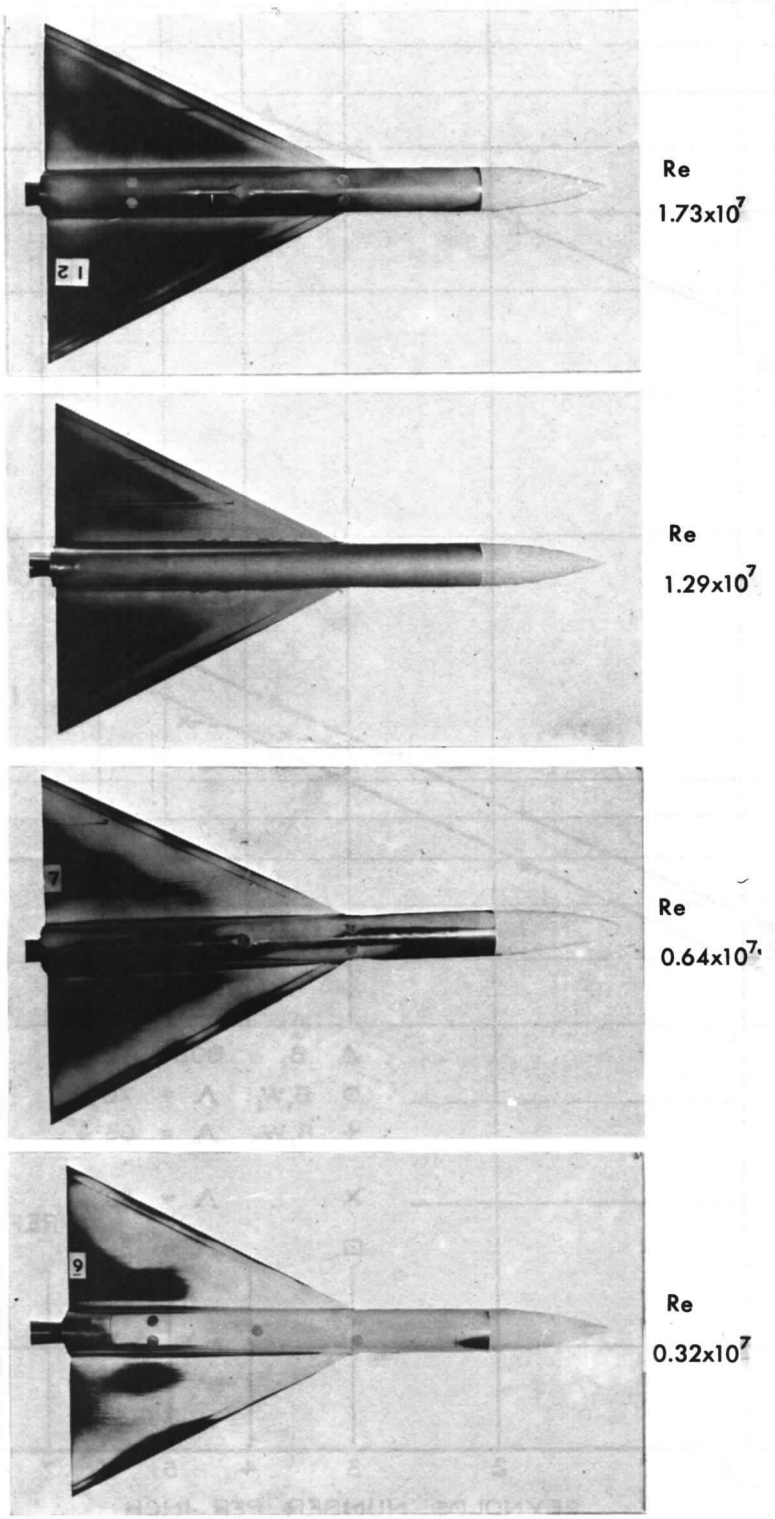

FIG. 5. Photographs taken following sublimation tests. Configuration $B_1\ W_3\ \alpha = 0°\ M = 4{\cdot}0$.

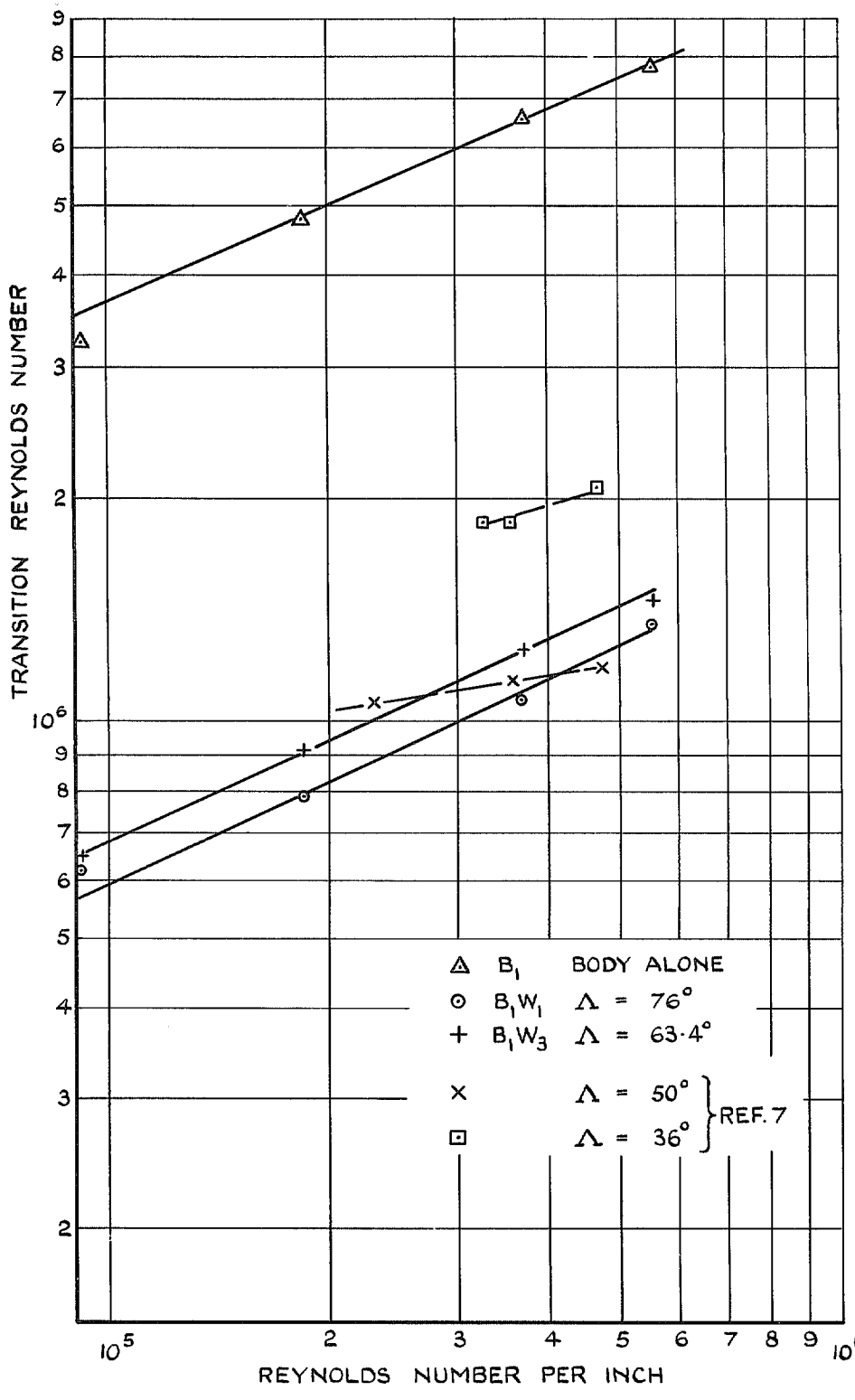

FIG. 6. Variation of transition Reynolds number with unit Reynolds number (obtained from photographs).

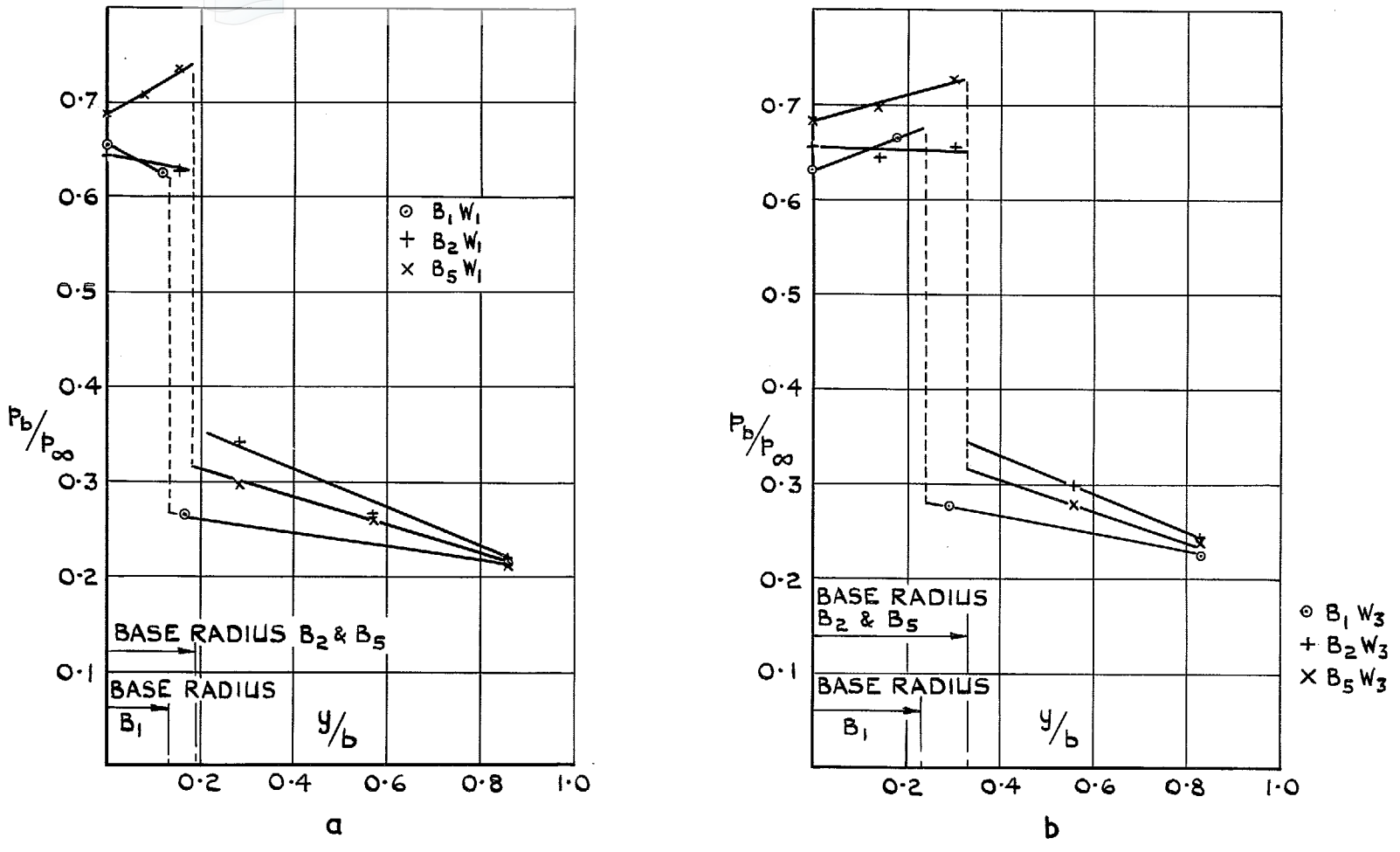

FIG. 7a & b. Base pressure measurements.

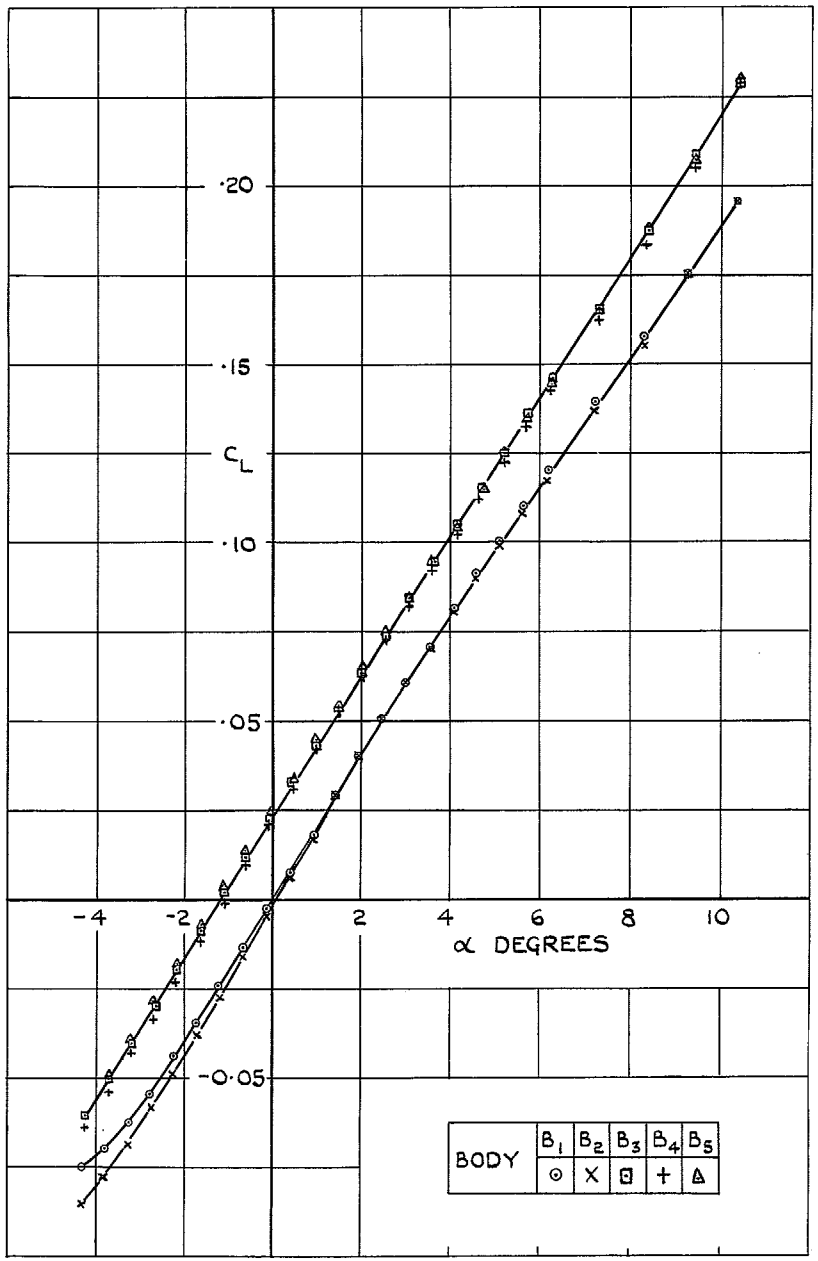

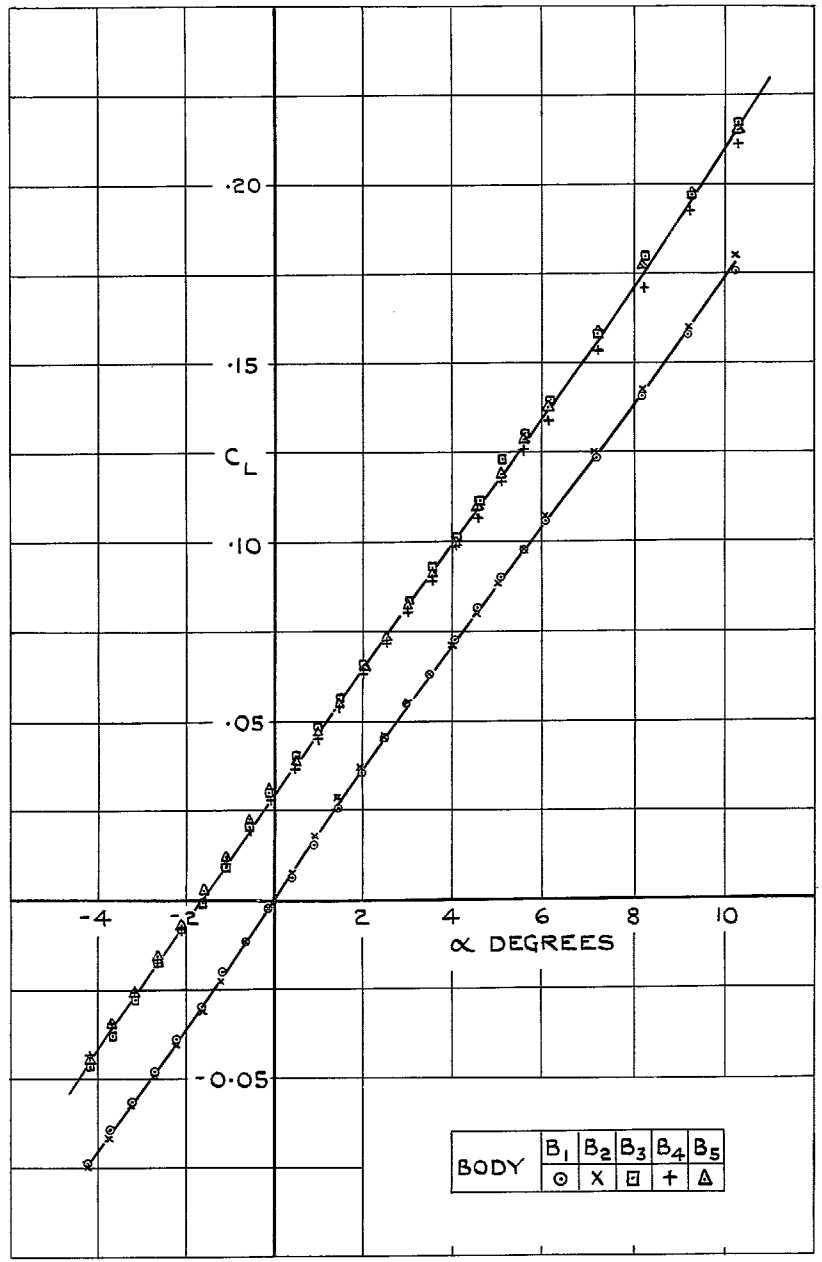

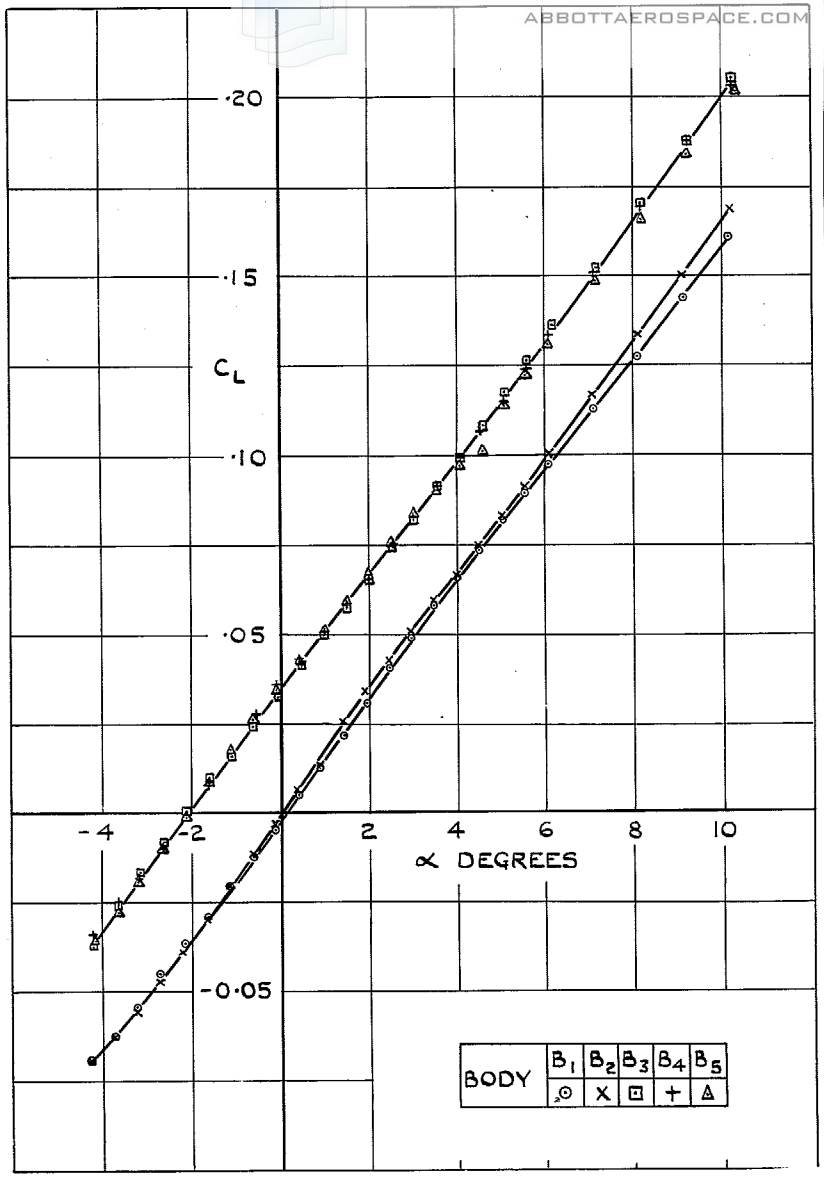

FIG. 10. Lift coefficient; wing W_3.

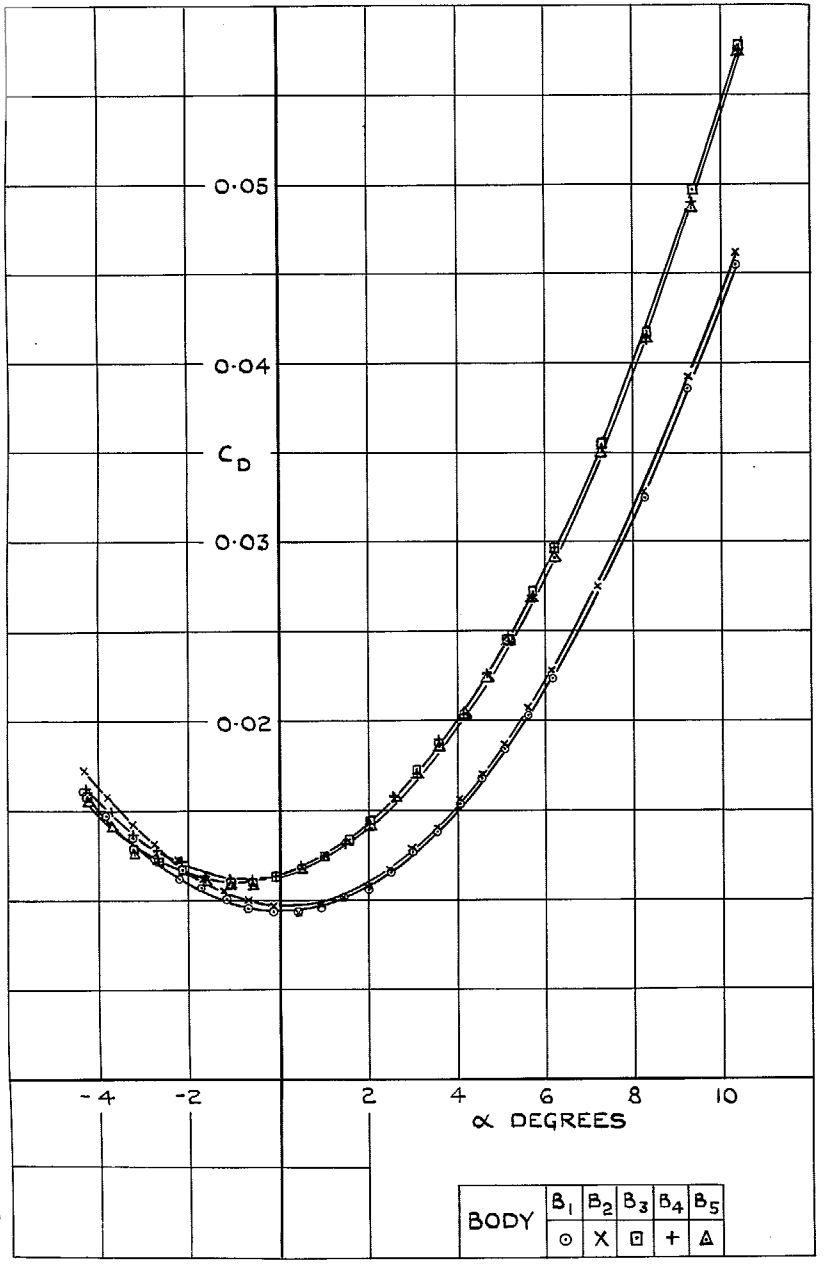

FIG. 11. Drag coefficient; wing W_1.

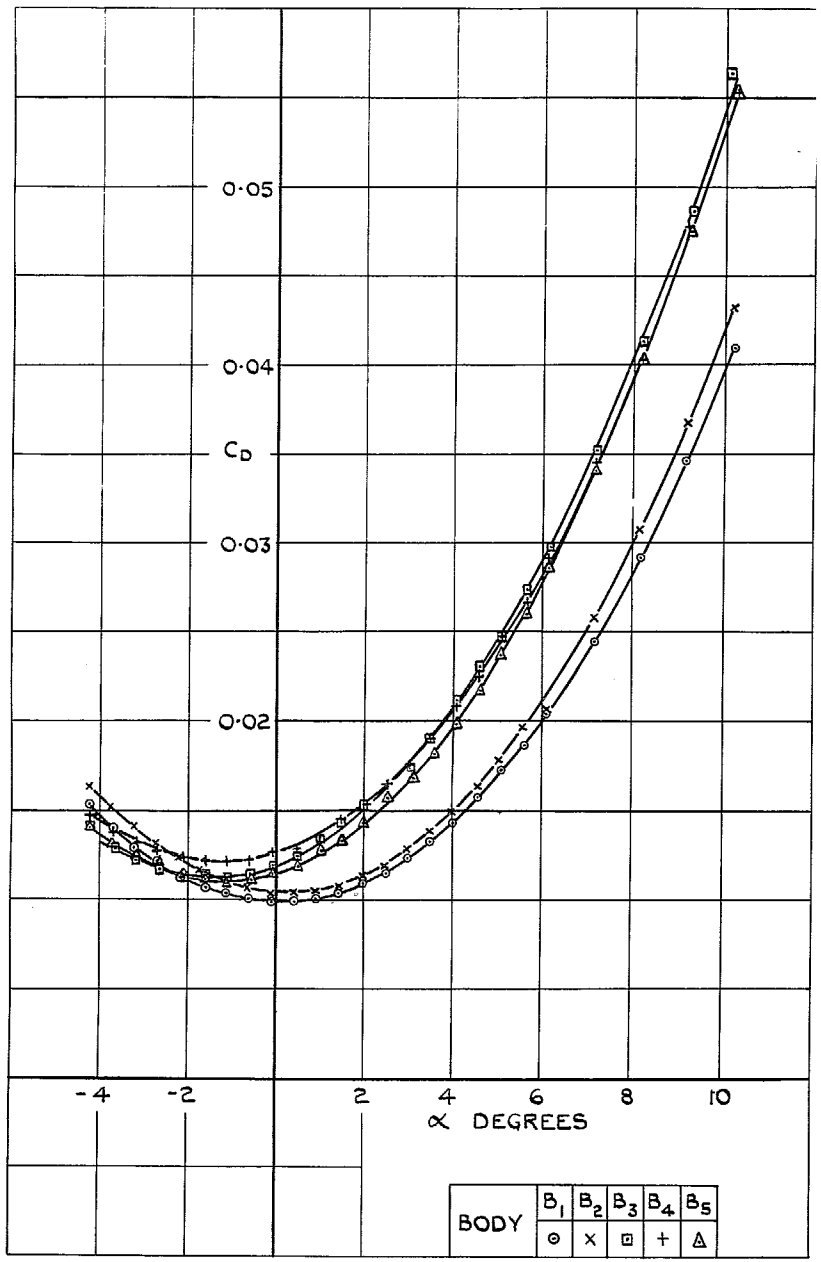

FIG. 12. Drag coefficient: wing W_2.

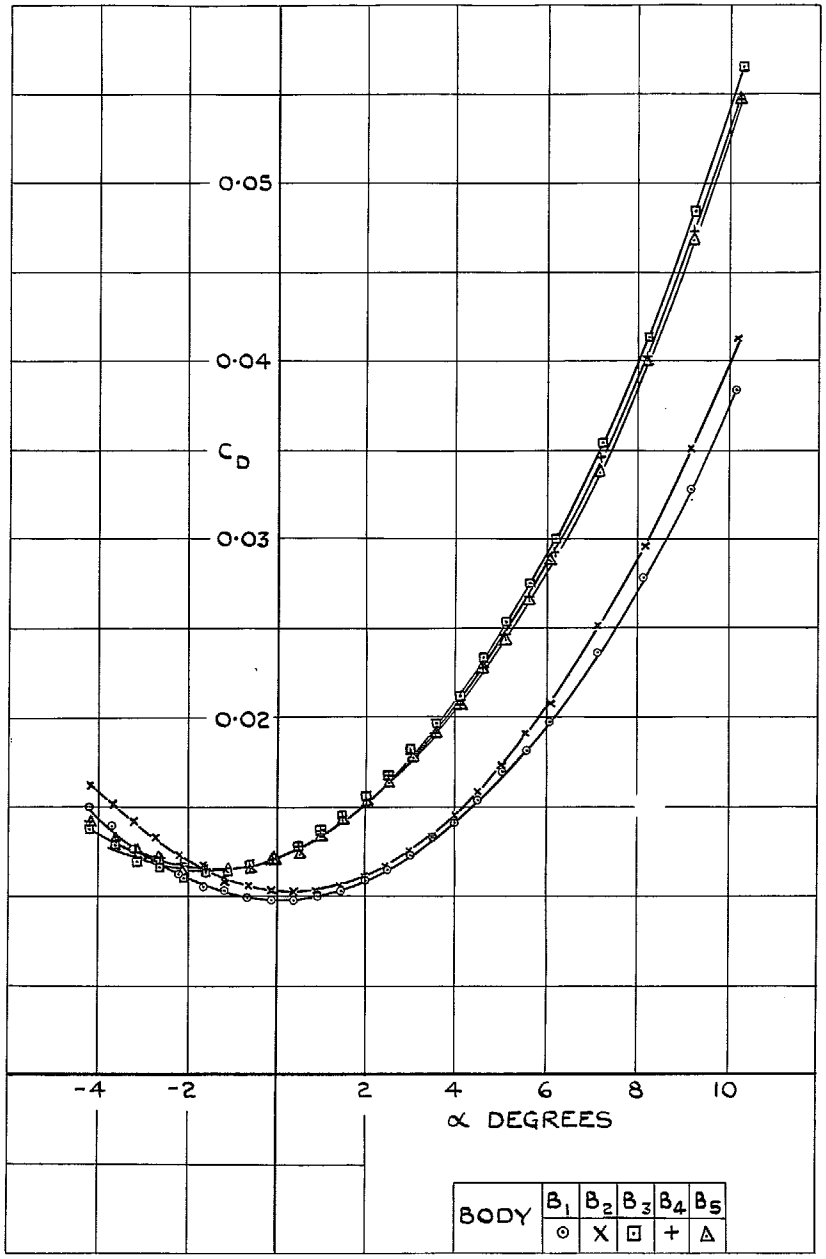

FIG. 13. Drag coefficient: wing W_3.

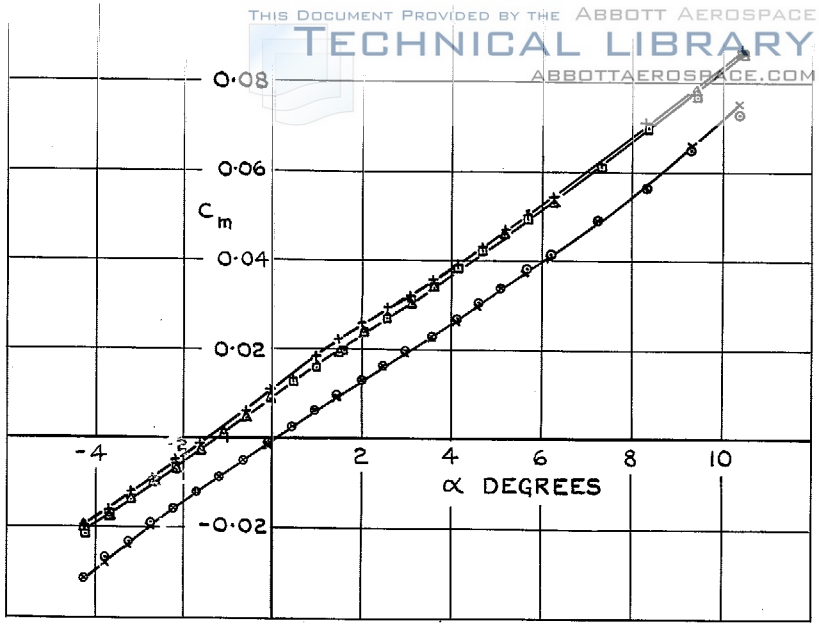

(a) PITCHING MOMENT

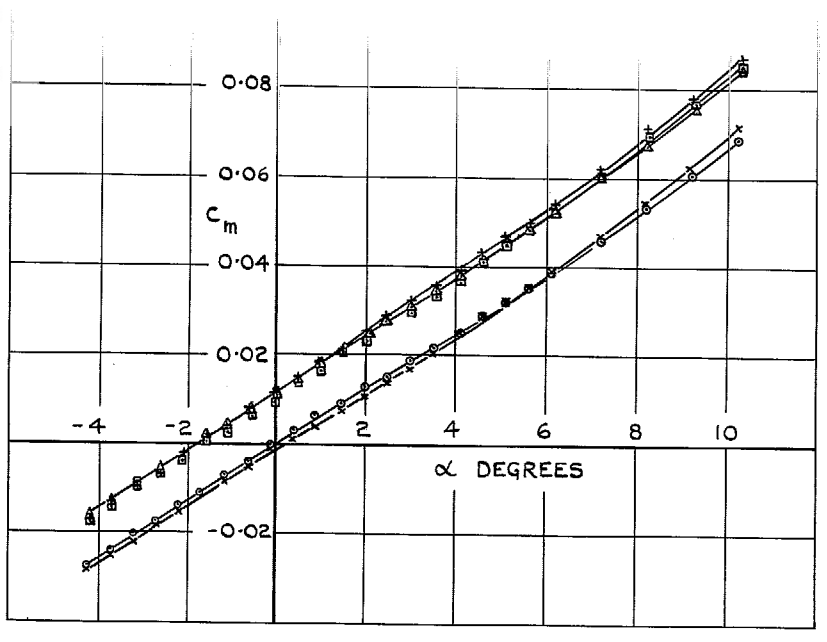

(a) PITCHING MOMENT

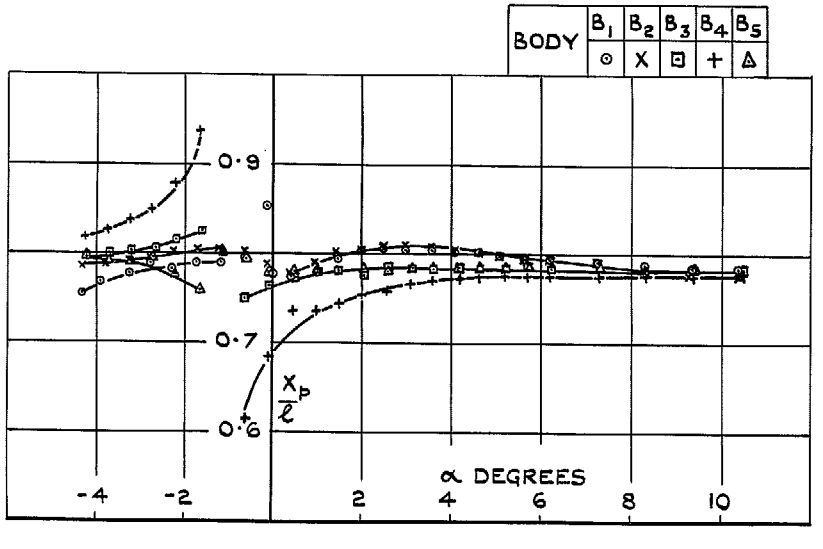

(b) CENTRE OF PRESSURE

FIG. 14a & b. Pitching moment and centre of pressure; wing W_1.

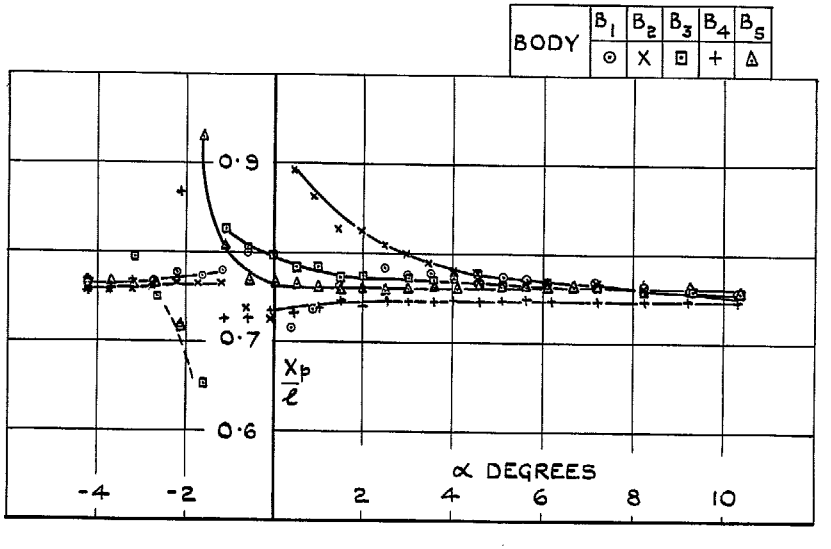

(b) CENTRE OF PRESSURE

FIG. 15a & b. Pitching moment and centre of pressure; wing W_2.

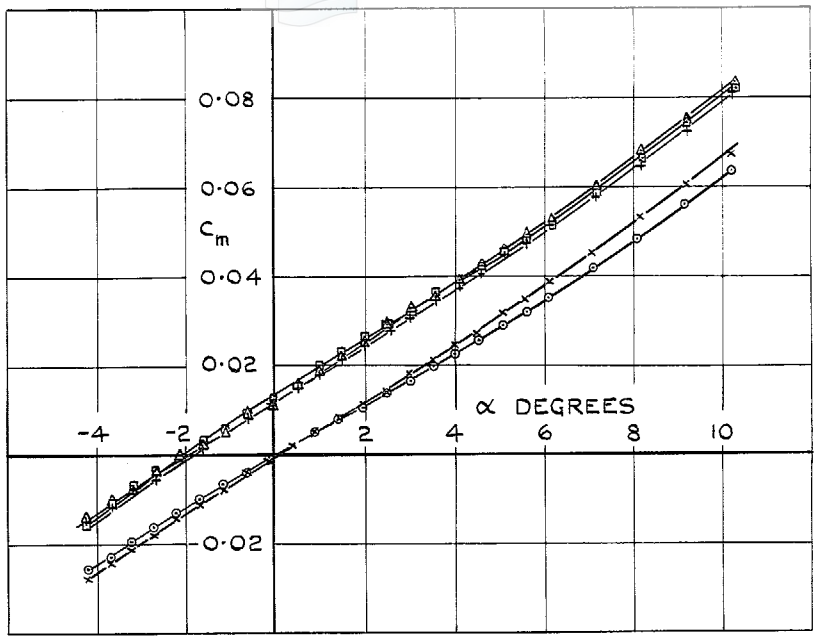

(a) PITCHING MOMENT

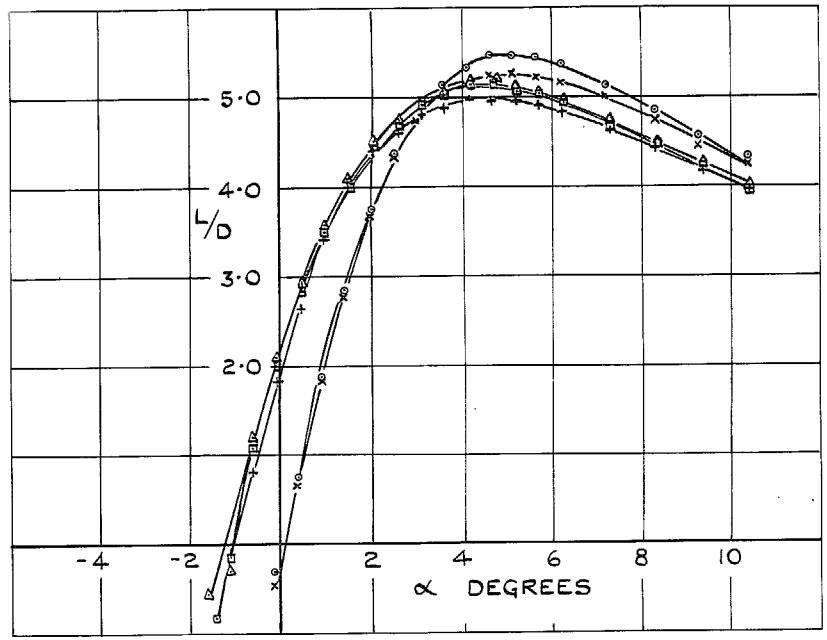

(a) WING W_1

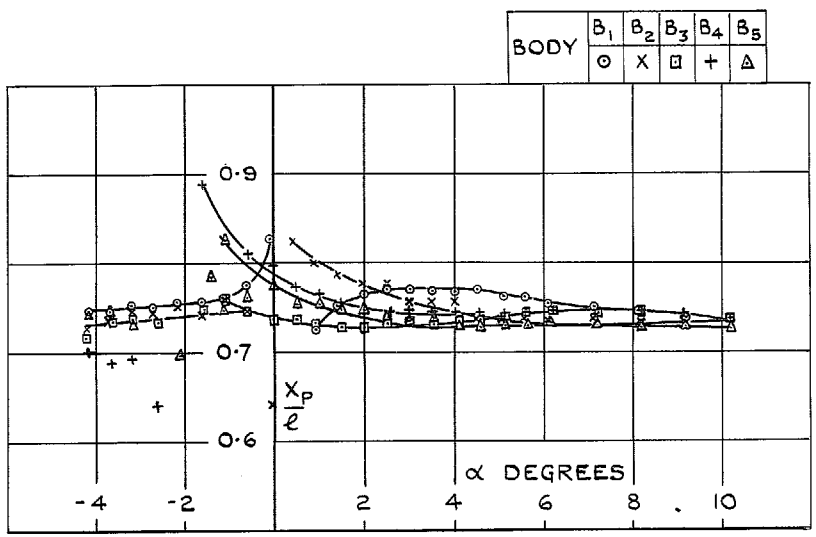

(b) CENTRE OF PRESSURE

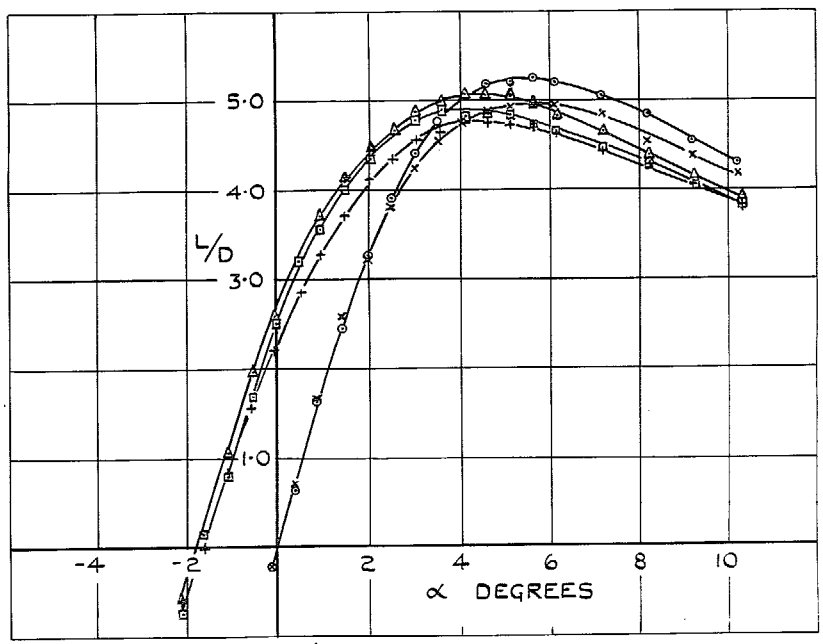

(b) WING W_2

FIG. 16a & b. Pitching moment and centre of pressure; wing W_3.

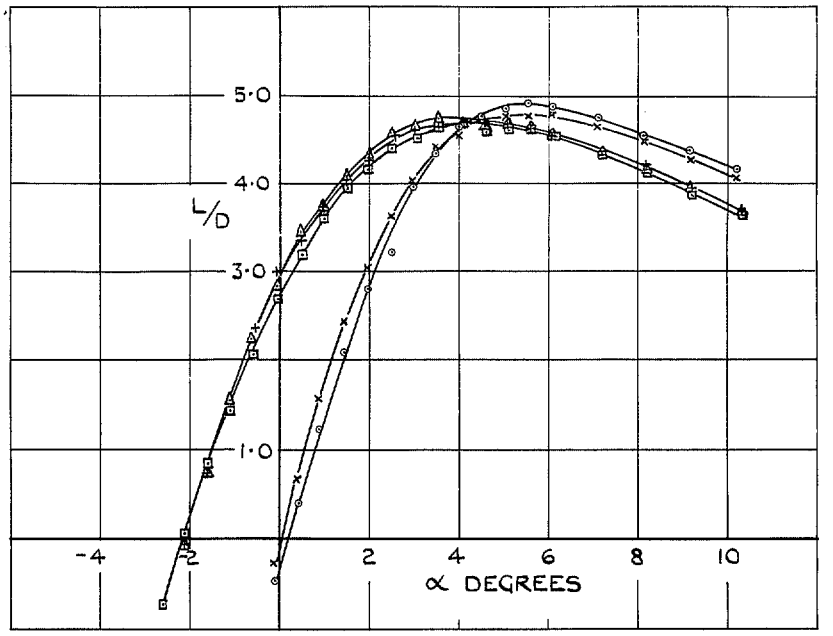

BODY	B_1	B_2	B_3	B_4	B_5
	⊙	X	⊡	+	△

(C) WING W_3

FIG. 17c. Lift to drag ratio (L/D).

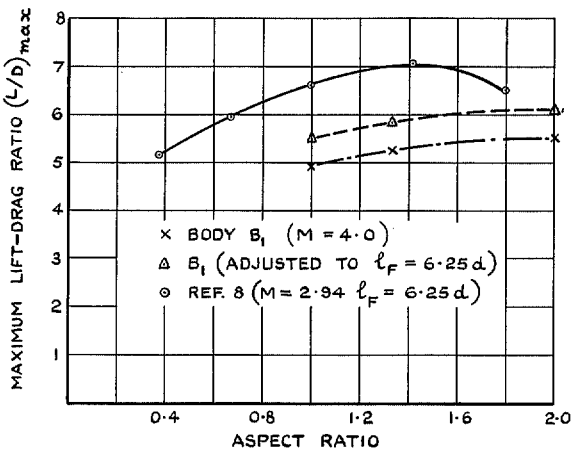

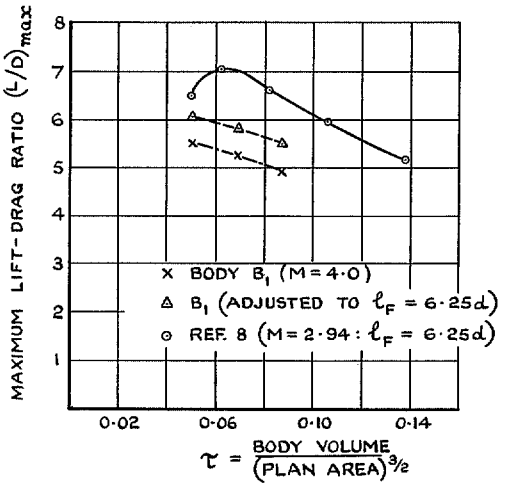

FIG. 18. Effect of aspect ratio and body volume on $(L/D)_{max}$.

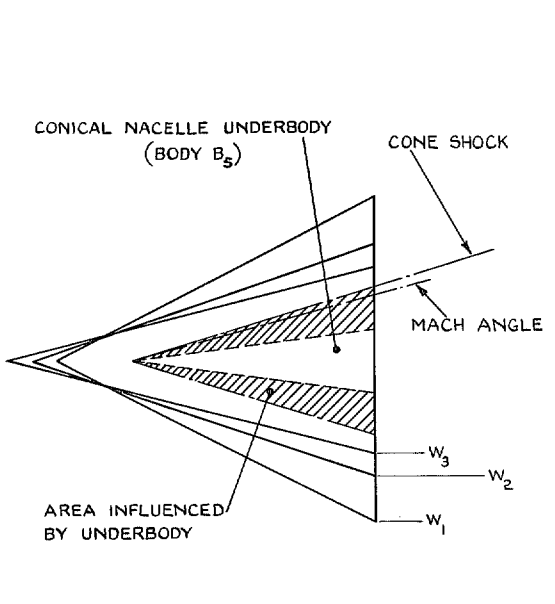

FIG. 19a. Relative extent of interference effect on the wings W_1, W_2 & W_3 due to body B_5.

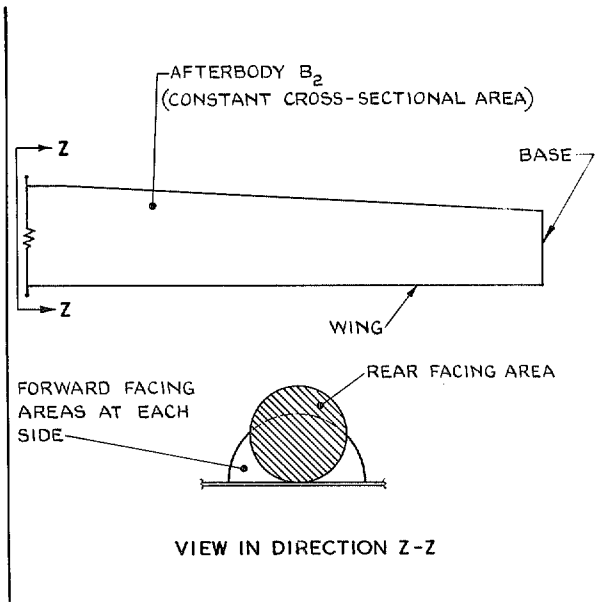

FIG. 19b. Forward and rear facing areas produced by changing shape of afterbody B_2.

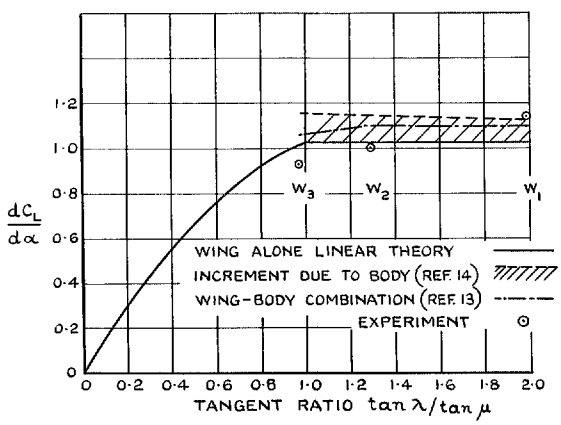

FIG. 20a. Comparison of experimental lift-curve slope with various theoretical predictions.

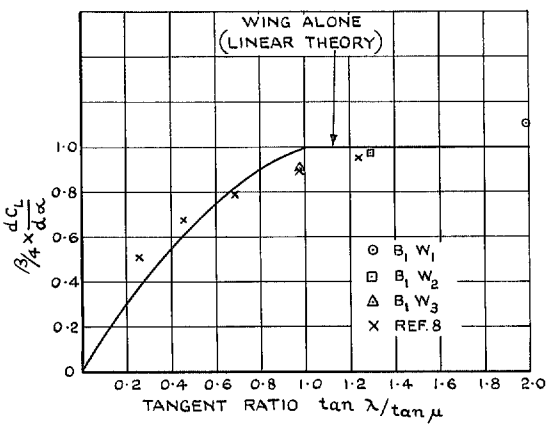

FIG. 20b. Comparison of experimental lift-curve slopes.

Printed in Wales for Her Majesty's Stationery Office by Allens Printers (Wales) Limited.
Dd. 146916. K.5.

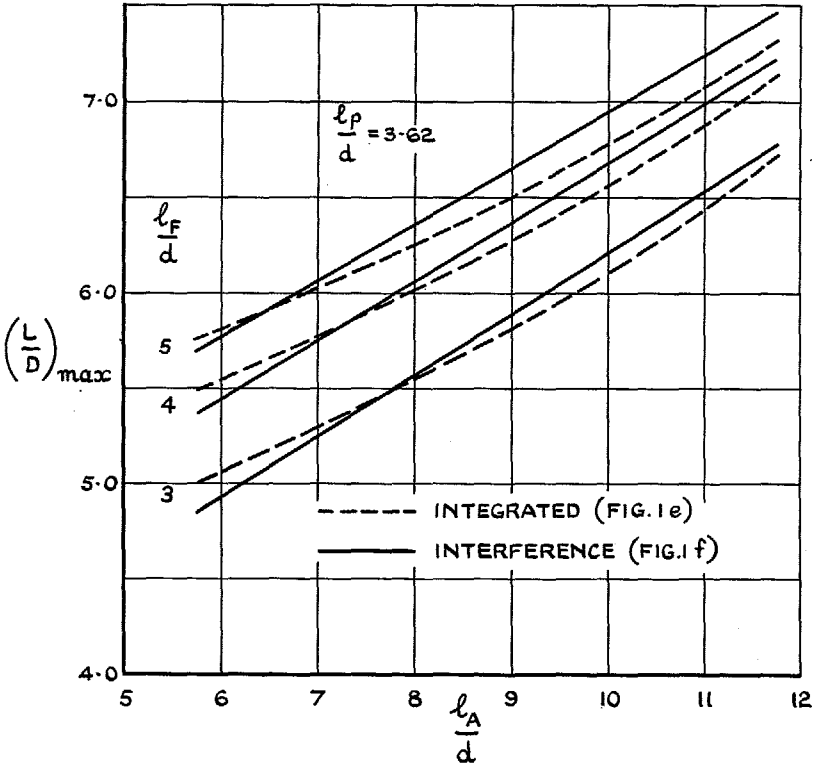

FIG. 21a. Theoretical variation of $\left(\frac{L}{D}\right)_{max}$ with afterbody fineness ratio.

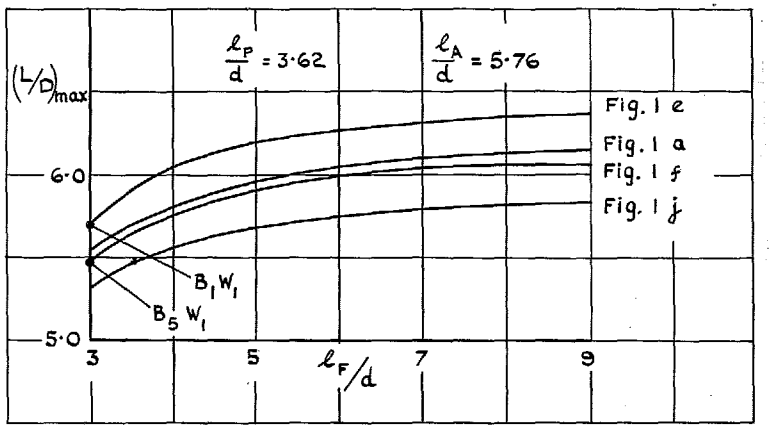

FIG. 21b. Theoretical variation of $(L/D)^{max}$ with forebody fineness ratio.

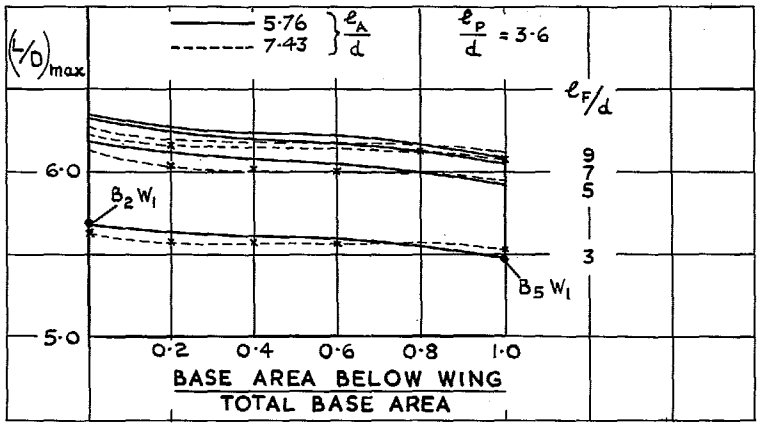

FIG. 21c. Theoretical variation of $(L/D)_{max}$ with proportion of base area below the wing.

Published by
HER MAJESTY'S STATIONERY OFFICE

To be purchased from
49 High Holborn, London WC1
13A Castle Street, Edinburgh EH2 3AR
109 St. Mary Street, Cardiff CF1 1JW
Brazennose Street, Manchester M60 8AS
50 Fairfax Street, Bristol BS1 3DE
258 Broad Street, Birmingham 1
7 Linenhall Street, Belfast BT2 8AY
or through any bookseller

SBN 11 470235 7